TORSIONAL STIFFNESS AND NATURAL FREQUENCY ANALYSIS OF A FORMULA SAE VEHICLE CARBON FIBER REINFORCED POLYMER CHASSIS USING FINITE ELEMENT ANALYSIS

A Thesis
presented to
the Faculty of California Polytechnic State University,
San Luis Obispo

In Partial Fulfillment
of the Requirements for the Degree
Master of Science in Mechanical Engineering

by
Manuel Herrmann
December 2016

COMMITTEE MEMBERSHIP

TITLE:	Torsional Stiffness and Natural Frequency Analysis of a Formula SAE Vehicle Carbon Fiber Reinforced Polymer Chassis using Finite Element Analysis
AUTHOR:	Manuel Herrmann
DATE SUBMITTED:	December 2016
COMMITTEE CHAIR:	Tom Mase, Ph.D. Professor of Mechanical Engineering
COMMITTEE MEMBER:	Joseph Mello, Ph.D. Professor of Mechanical Engineering
COMMITTEE MEMBER:	Sthanu Mahadev, Ph.D. Assistant Professor of Mechanical Engineering

ABSTRACT

Torsional Stiffness and Natural Frequency Analysis of a Formula SAE Vehicle Carbon Fiber Reinforced Polymer Chassis using Finite Element Analysis

Manuel Herrmann

Finite element is used to predict the torsional stiffness and natural frequency response of a FSAE vehicle hybrid chassis, utilizing a carbon fiber reinforced polymer sandwich structure monocoque and a tubular steel spaceframe. To accurately model the stiffness response of the sandwich structure, a series of material tests for different fiber types has been performed and the material properties have been validated by modeling a simple three-point-bend test panel and comparing the results with a physical test. The torsional stiffness model of the chassis was validated with a physical test, too. The stiffness prediction matches the test results within 6%. The model was then used to model the natural frequency response by adding and adjusting the materials' densities in order to match physical mass properties. A hypothesis is made to explain the failure of the engine mounts under the dynamic response of the frame.

Keywords: FSAE, FEA, Chassis, CFRP, Torsional Stiffness, Natural Frequency

ACKNOWLEDGMENTS

Firstly, I would like to thank my committee for giving me the chance of exploiting my passion for finite element analysis and composites. My special thanks goes to my advisor Dr. Tom Mase who was brave enough to support me with this Master's thesis and being a guide through the whole project. I would like to thank Dr. Joseph Mello for introducing me to composites that kept fascinating me over the whole period of this thesis and beyond. I would like to thank Dr. Mahadev Sthanu for his advice on both composites and finite element analysis, that helped me bring this work to a successful end. Additionally, I would like to thank Dr. Peter Schuster for his advice on how to successfully wrestle with Abaqus and Dr. Hemanth Porumamilla who helped me with his experience in the field of vibrations.

Secondly, I would like to thank Jim Johnson from VPG micromeasurements for the donation of all the strain gauges and applicator that has been used for the material tests.

Thirdly, I would like to thank the team of FSAE Cal Poly Racing and my fellow grad students for an amazing time and incredible college experience which lead me to this thesis in the first place. Specifically, Ruben Diaz, Nathan Powell, Nicholas Gholdoian, Journey McDowell, Mike Kramerz, Esther Unti, Kevin Ziemann, Ford Eimon, Adam Menashe and Gina Ghiglieri who I have spent countless hours in the lab with, providing constant motivation and inspiration. They have been like a family to me and for that I am eternally thankful.

Last but certainly not least, I would like to thank my family and my girlfriend for their endless love and support this whole time. They gave me the energy to keep going when I was about to give up. Without them, I would not be where I am today and for that I am forever grateful.

TABLE OF CONTENTS

Page

LIST OF TABLES x

LIST OF FIGURES xii

LIST OF UNITS AND VARIABLES xv

CHAPTER

1. INTRODUCTION 1

    1.1 Literature Research 2

        1.1.1 Chassis Stiffness 2

            1.1.1.1 Longitudinal Torsion 3

            1.1.1.2 Vertical Bending 4

            1.1.1.3 Lateral Bending 5

            1.1.1.4 Horizontal Lozenging 5

        1.1.2 Chassis Natural Frequency 7

    1.2 Objective 9

2. BASIC MATERIAL PROPERTIES 10

    2.1 Carbon Fiber Reinforced Polymer 10

        2.1.1 Material Constituents 10

        2.1.2 Material Testing 14

            2.1.2.1 Tensile Tests 14

2.1.2.2 In-Plane Shear Tensile Tests 19
2.1.3 Composite Testing Results 22
2.2 Aluminum Honeycomb Material Properties 23
2.2.1 Honeycomb Properties - Experimental Method 24
2.2.2 Honeycomb Properties – Analytical Method 25
2.2.3 Honeycomb Properties – Numerical Method 26
2.2.4 Summary of the Honeycomb Properties 31
3. COMPONENT SCALE VALIDATION OF THE MATERIAL PROPERTIES 33
3.1 Physical Test 33
3.1.1 Panel Manufacturing 33
3.1.2 Test Setup 34
3.1.3 Component Test Validation 35
3.2 Simulation of the Component Test 36
3.2.1 Preliminary Sizing 36
3.2.2 Component Modeling and Simulation 38
3.2.2.1 Pre-Processing 38
3.2.2.2 Element Choice and Mesh 39
3.2.2.3 Post-Processing 40
3.2.2.4 Modeling Issues Encountered 41
3.3 Results and Conclusion 42
4. CHASSIS TORSIONAL STIFFNESS MODEL 44
4.1 Chassis Torsional Test 44

4.1.1 Test Setup 44
4.1.2 Torsion Test Process 46
4.1.3 Torsion Test Results 46
4.2 Modeling and Simulation 47
4.2.1 Geometry 48
4.2.1.1 Monocoque 48
4.2.1.2 Tubular Spaceframe 49
4.2.1.3 Suspension 51
4.2.1.4 Engine 52
4.2.2 Mesh and Element Choice 54
4.2.3 Connector Elements and Constraints 56
4.2.4 Boundary Conditions and Analysis Type 57
4.2.5 Modeling Issues Encountered 58
4.2.6 Chassis Torsion Simulation Results 59
4.2.7 Comparison and Discussion 60
4.2.8 Stiffness Distribution 61
5. CHASSIS NATURAL FREQUENCY MODEL 63
5.1 Preliminary Considerations 63
5.2 Mass Properties and Scaling 64
5.3 Boundary Conditions and Constraints 66
5.4 Results and Discussion 67
5.5 Modal Analysis Conclusion 71

6. CONCLUSION.....74

7. FUTURE WORK.....77

BIBLIOGRAPHY.....78

APPENDICES

APPENDIX A.....84

APPENDIX B.....89

APPENDIX C.....93

LIST OF TABLES

Table Page

Table 1: Fiber direction tensile test specimen dimensions and results 18

Table 2: Transverse direction tensile test specimen dimensions and results 19

Table 3: In-plane shear test specimens dimensions 21

Table 4: Averaged material properties and comparison to vendor data 22

Table 5: Engineering constants for the core from vendor [31] 24

Table 6: Cell segment dimensions 27

Table 7: Results for the effective material properties of the core 31

Table 8: Summary of calculated effective properties for the honeycomb core 31

Table 9: Engineering constants that satisfy compliance matrix restrictions 32

Table 10: Results of the three-point-bend test models 42

Table 11: Overview of the layup sections 49

Table 12: Profile cross section overview 50

Table 13: Overview of profile sections for the suspension 52

Table 14: Comparison between model and physical test 60

Table 15: Torsional stiffness of the chassis with rigid components 61

Table 16: Material density and scaled density 65

Table 17: Natural frequency results from the first run 67

Table 18: Natural frequency results from the second run.....68

Table 19: Natural frequency results from the third run 69

Table 20: Natural frequency results from the fourth run.....70

LIST OF FIGURES

Figure Page

Figure 1: Longitudinal Torsion Deformation Mode [2] 3

Figure 2: Vertical Bending Deformation Mode [2] 4

Figure 3: Lateral Bending Deformation Mode [2] 5

Figure 4: Horizontal Lozenging Deformation Mode [2] 5

Figure 5: Material Coordinate System in a Lamina [20] 10

Figure 6: Stress-Strain curve for test number 1.2 16

Figure 7: Normal Strain vs Transverse Strain curve for test number 1.2 17

Figure 8: Shear Strain vs Shear Stress curve for test number 1.15 20

Figure 9: Single honeycomb cell [30] 24

Figure 10: Geometry of the honeycomb structure [34] 25

Figure 11: Deformation under in-plane shear load [34] 25

Figure 12: (a) Plan view of hexagonal cell core; (b) Unit cell [29] 27

Figure 13: (a) 3-D view of unit cell; (b) 1/8 segment used for modeling [29] 27

Figure 14: Labelled edges and surfaces for boundary conditions [29] 28

Figure 15: Boundary Conditions for different loading cases based on [29] 29

Figure 16: Mesh convergence study for the cell segment 30

Figure 17: Structure of the sandwich panel 34

Figure 18: Three-point-bend test [1] 35

Figure 19: Test fixture....35

Figure 20: Load vs Displacement curve....36

Figure 21: Failed test panel 36

Figure 22: Stiffness sensitivity of the panel to ply thickness....37

Figure 23: Stiffness sensitivity of the panel to core thickness 37

Figure 24: Component Simulation Boundary Conditions....38

Figure 25: Mesh sizing in the contact area 39

Figure 26: Z-Deflection of the panel with solid core elements 41

Figure 27: Local penetration of the panel in a center plane cut view....42

Figure 28: 2016 chassis on the torsional test fixture 45

Figure 29: Gauge to measure the deflection at the front left upright....45

Figure 30: Average applied torque vs torsional stiffness curve 47

Figure 31: Layup sections of the monocoque [38] 48

Figure 32: Tubing profiles of the rear spaceframe and roll hoop [38] 50

Figure 33: Final chassis model within Abaqus 53

Figure 34: Mesh convergence plot for the monocoque 54

Figure 35: Mesh convergence plot for the spaceframe 55

Figure 36: Boundary conditions of the chassis model....57

Figure 37: Contour plot of the z-deflection 59

Figure 38: Overview of the boundary conditions 66

Figure 39: Frequency results for the engine point mass study 71

Figure 40: Shape of the 1st torsional mode 72

Figure 41: Shape of the 2nd torsional mode 73

LIST OF UNITS AND VARIABLES

INTERNATIONAL SYSTEM OF UNITS (METRIC)

mm: millimeter

N: newton

Hz: Hertz

U.S. CUSTOMARY UNITS (ENGLISH)

in: inch

ft: feet

lb_f: pounds force

lb_m: pounds mass

psi: pounds per inch

ksi: kilopounds per inch

Msi: megapounds per inch

F: Fahrenheit

rpm: revolutions per minute

deg: degree

rad: radian

mph: miles per hour

inHg: inches of mercury

GREEK VARIABLES

σ: stress

τ: shear stress

ε: strain

μ: micro (10^{-6})

γ: shear strain

ν: Poisson's ratio

θ: angle

δ: deflection

ρ: density

ω: rotational natural frequency

LATIN VARIABLES

m: mass

C: stiffness constants

E: Young's modulus

G: shear modulus

S: compliance constants

k: stiffness

k_t: torsional stiffness

h: height

l: length

t: thickness

t_{ply}: ply thickness

t_{core}: core thickness

u: displacement

F: force

L: initial length

A: area

a: wall width

d: distance

T: torque

f: frequency

I_p: moment of inertia

1. INTRODUCTION

For the 2015/2016 season the Cal Poly Formula SAE Racing Team decided to merge the Formula Electric and the Formula Combustion team and build both cars on a uniform platform. The design utilizes a hybrid chassis with an interchangeable tubular space-frame to house power unit and drivetrain combined with a driver cell that is constructed as a mono-coque made from carbon fiber skins and aluminum honeycomb core. The design has been chosen to take advantage of the high stiffness-to-weight ratio of a carbon fiber sandwich structure combined with the easy accessibility of a spaceframe to service drivetrain components.

The torsional stiffness of the chassis has been the driving parameter for the design of the structure and the laminate of the monocoque. Attempts have been made in the past to utilize Computer Aided Engineering (CAE) tools to predict overall torsional stiffness of the chassis in order to define the laminate of the monocoque to be as light as possible while meeting the necessary stiffness, strength and energy absorption requirements of the rules [1]. The results predicted a significantly higher torsional stiffness compared to data from a physical test, leaving the team with no other choice than conservative assumptions and extensive testing, which is time consuming, expensive and leads to an overbuilt chassis. A better understanding of the chassis' stiffness is necessary to improve the design of the chassis and decrease the weight of the chassis.

Another concern arose from cracking engine mounts during the 2014/2015 season, assumed to be caused by the excitation of unbalanced mass from the engine and matching resonant frequencies of the chassis, causing high transmissibility and high stresses, respectively. A better understanding of the systems vibration normal modes is necessary

to find out if resonance is the cause for the cracking mounts and what actions are necessary to prevent damage in the engine mounts in upcoming seasons.

1.1 Literature Research

1.1.1 Chassis Stiffness

The stiffness of a racecar chassis has significant effects on the dynamic and handling characteristics of the vehicle. The goal is to design a chassis that is just stiff enough so that changes in the suspension setup makes a notable change in the handling characteristics of the car while keeping the weight as low as possible. A lot of work has been done on answering the question of “how stiff is stiff enough?” [2 - 6].

One way of approaching this problem is to determine the best way of transferring the loads from the suspension through the structure and the mode of deformation that is associated with these loads. By connecting the deformation to the change in handling characteristics of the vehicle, a stiffness target can be defined for each deformation mode. Heisler [7] gives the main deformation modes for an automotive chassis being:

1. Longitudinal Torsion
2. Vertical Bending
3. Lateral Bending
4. Horizontal Lozenging

1.1.1.1 Longitudinal Torsion

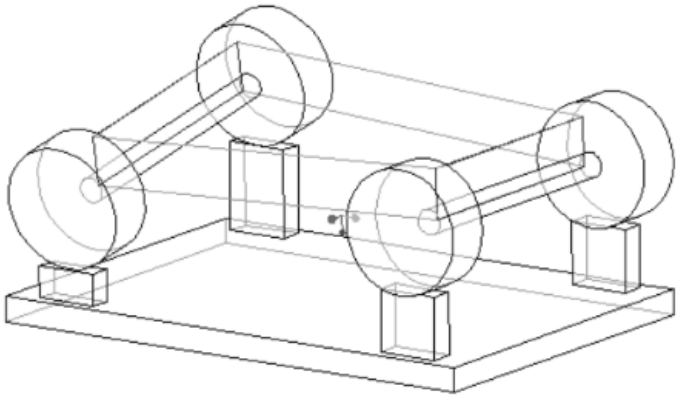

Figure 1: Longitudinal Torsion Deformation Mode [2]

Torsional loads on the chassis result from the suspension forces acting in opposite corners of the car, which is the case when the car is cornering. The frame that is connecting the front and rear suspension acts as a torsional spring in between and is influencing the difference in roll angle between front and rear [3]. The difference in roll angle, or the torsional deformation of the frame is inversely proportional to the frame's torsional stiffness.

To make the vehicle handle correctly, it must be possible to tune the handling balance [4]. That is mainly done by changing the roll stiffness between the front and the rear of the suspension, since it transfers directly to the lateral load transfer distribution that dictates how the normal load on the tires change due to lateral acceleration. The satisfactory torsional stiffness of the chassis is therefore dictated by the allowable difference in front to rear lateral load transfer compared to the values the suspension is set up for [4].

1.1.1.2 Vertical Bending

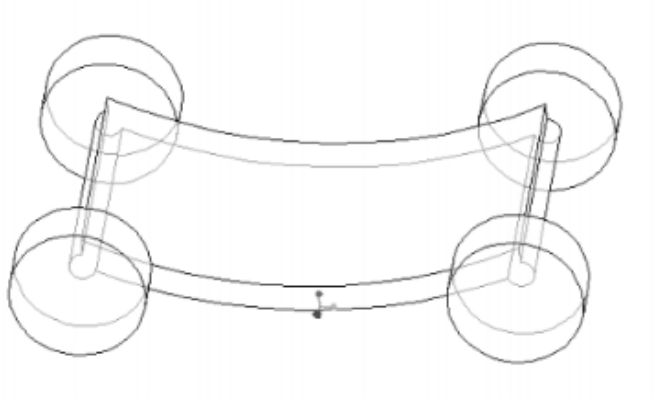

Figure 2: Vertical Bending Deformation Mode [2]

Loads that induce vertical bending arise from the weight of the driver and heavy components like the engine that are attached to the frame. However, those loads are static and don't change due to dynamic actions of the car. More importantly, forces due to accelerations and decelerations of the car causing longitudinal load transfer that changes the normal load on the tires, also referred to as dive and squat behavior [6].

Varying normal load on the tires leads to fluctuations in longitudinal and lateral forces, impacting the cars handling performance. This affects mostly combined cases, like the acceleration out of a corner or braking in turn, where longitudinal load transfer and lateral load transfer occur simultaneously.

Dive and squat behavior are also a function of the suspension setup and can be tuned in during the suspension setup. It can be seen that for both cases, the chassis stiffness is a function of the stiffness of the suspension.

1.1.1.3 Lateral Bending

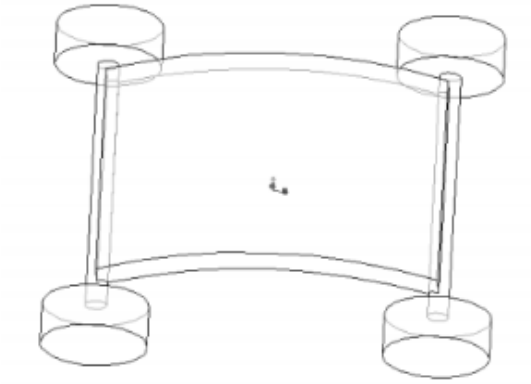

Figure 3: Lateral Bending Deformation Mode [2]

Sideways forces that cause the chassis to bend in the lateral direction are induced by road camber, side wind loads and centrifugal forces caused by cornering [2]. The lateral bending of the chassis doesn't affect the handling characteristics significantly and can be neglected.

1.1.1.4 Horizontal Lozenging

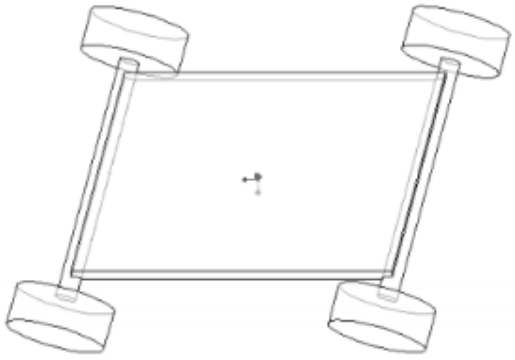

Figure 4: Horizontal Lozenging Deformation Mode [2]

Unequal longitudinal forces between the front and rear axle cause a compression or elongation of the frame. Those forces arise during acceleration and braking because of a longitudinal weight transfer to rear, in terms of acceleration and to the front in terms of braking. This type of deformation however, doesn't affect the handling characteristics of the car and can also be neglected.

Comparing those four modes of deformation it can generally be stated that torsional and vertical bending stiffness are the two most important parameters to design for, to achieve satisfactory handling characteristics. Moreover, it has been found that a frame that has satisfactory torsional stiffness also has satisfactory vertical bending stiffness [8]. Therefore, further investigation focuses solely on the torsional stiffness of the chassis.

Different methods have been found to determine the torsional stiffness target for a given suspension setup. In [2] a ratio between the torsional stiffness of the chassis and a rigid chassis relative to the suspension roll stiffness is used to determine a satisfactory stiffness value for the chassis. It is important to note that chassis stiffness is the sum of two springs in series, namely the frame stiffness and the stiffness the suspension excluding the coil springs.

The results of [3] show that the main effect of torsional stiffness is steady-state difference in roll angles. They propose a "matching principle of suspension roll stiffness" for steady-state considerations where the torsional stiffness is determined by the tuned in difference in roll angle between front and rear suspension.

In [4], different suspension stiffness's are exploited with different chassis stiffness's to determine the loss in roll stiffness due to torsional flex of the frame for a static analysis. An equation was found that can be used to estimate the ratio of total chassis roll stiffness to chassis torsional stiffness for a given acceptable loss in percent of roll stiffness

distribution ratio. Additionally, a dynamic analysis has been performed that showed how the distribution of torsional stiffness along the length of the chassis is affecting the handling of the vehicle. Torsionally compliant regions of the chassis close to the suspension can reduce the roll stiffness of the suspension.

In order to predict an accurate torsional chassis stiffness, it is therefore important to pay attention to stiffness of suspension and frame. Additionally, the stiffness distribution along the length of the chassis is an important parameter to evaluate optimization potential. The Finite Element Method (FEM) is well suited for this type of analysis and has been utilized to predict torsional stiffness in [2, 9 - 15].

1.1.2 Chassis Natural Frequency

Besides the handling performance of a race car, chassis stiffness and weight are also a driving factor for the natural frequency response of structure. Determining the natural frequencies can therefore be used to determine the stiffness-to-weight ratio of the chassis, as suggested in [11]. The natural frequency is the response of a structure when perturbed by external forces and is defined as follows:

$$\omega_n = \sqrt{\frac{k}{m}}. \tag{1.1}$$

A lot of the stiffness values for the chassis are torsional stiffness for which the natural frequency calculates to:

$$\omega_n = \sqrt{\frac{k_t}{I_p}}. \tag{1.2}$$

Respectively, a chassis with a high stiffness-to-weight ratio has high natural frequencies and the other way around.

Besides having a measure for the stiffness-to-weight ratio, knowing natural frequencies of a system is also important to ensure that various dynamic load inputs don't match resonant frequencies. Load inputs can be unbalanced rotating masses like the wheels and the engine, or load variations at the wheels due to the surface roughness of the road. If the frequency of those excitations are close to one of the natural frequencies of the chassis, it will oscillate according to the mode of deformation that is matched, causing the loads that are transferred into the system to increase and cause damage to the parts involved. It is therefore desired to have a chassis with frequencies that are higher than the various excitations. Frequencies that are an octave apart from each other, don't interfere with each other and can therefore be treated as individual systems [16].

The chassis consists of multiple bodies that all have different natural frequencies and multiples, also referred to as "harmonics". Therefore, an infinite amount of natural frequencies exists for the chassis. However, it is only important to know the lower frequencies with high amplitudes and strain energy. The frequency of the suspension is driven by the stiffness of the shocks and is typically in the range of 2 – 5 Hz [8]. Typical values for the first natural frequency for an FSAE race car chassis were found around 60 Hz to 120 Hz for a chassis torsional stiffness of around 1500 ft-lb/deg with a weight of around 80 lb [11], [17].

An easy way of determining the natural frequencies and accompanying modes of deformation is a free-free dynamic analysis using Finite Element Method, as in [18] - [19].

1.2 Objective

The goal of this thesis was to develop a process to model the torsional stiffness of the chassis using Abaqus CAE finite element analysis software and to match the results to a physical test. Furthermore, the natural frequencies and normal modes were investigated to determine if the frequency range intersects with the excitation frequencies of the engine. This was done by gathering the necessary material properties and evaluating them in a physical three-point-bend test with a simple sandwich panel. Next, a model of the chassis was developed and validated by comparing it to the results from a physical test. The model was then used to break down the structure into its components to investigate the stiffness of each member of the chassis, using a simple springs-in-series model, to gain a better understanding of the system. Utilizing the validated torsional stiffness model, masses were tuned to match the measured mass properties of the vehicle to determine the natural frequencies and the affiliated modes. The frequencies were then compared to the engine's excitation frequencies to determine if resonance was the cause of the cracking mounts.

2. BASIC MATERIAL PROPERTIES

While steel and aluminum are isotropic materials that are well characterized and understood, carbon fiber reinforced polymer (CFRP) is still an area of active research. This is mainly due to its non-isotropic behavior and the fact that the manufacturing process has a big impact on the material properties. Besides CFRP, aluminum honeycomb core is utilized in the sandwich structure the monocoque is made of. Despite the material of the core being aluminum, its behavior is highly non-isotropic due its microstructure and must be modeled as such. In order to build a material database for the simulation, it is necessary to get reliable material properties. Determining reliable material properties is the objective of this chapter.

2.1 Carbon Fiber Reinforced Polymer

2.1.1 Material Constituents

CFRP is a composite material constructed from carbon fiber embedded in a resin matrix, used to keep the fibers in place and bond them together. In a unidirectional ply, continuous fibers are all oriented in the same direction, as can be seen in Figure 5.

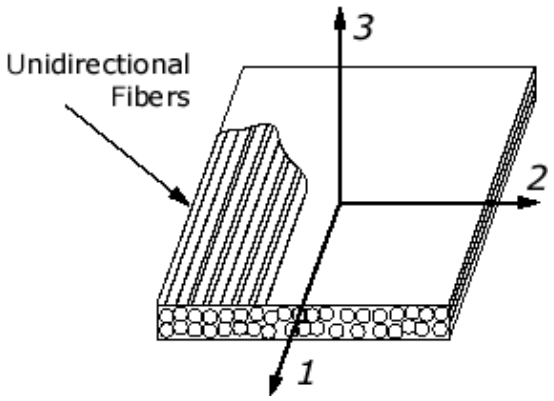

Figure 5: Material Coordinate System in a Lamina [20]

Since the stiffness and strength of the fiber is usually significantly higher than the resin, the lamina is stiffer and stronger in the direction of the fiber orientation (1-direction) than in the transverse direction (2 direction) and the out-of-plane direction (3-direction). This is why laminae are considered anisotropic.

The elastic behavior of an anisotropic material can be described by the generalized Hooke's law, that relates stress to strain by using a fourth order tensor E_{ijkl} [21] in indicial notation,

$$\sigma_{ij} = E_{ijkl}\varepsilon_{ij}. \tag{2.1}$$

The elastic tensor E_{ijkl} can have up to 81 elastic constants. Fiber composites generally fall under a specific category of anisotropic materials, called orthotropic materials, which possess three material symmetry planes. For an orthotropic material this tensor can be reduced to nine independent non-zero constants, since the invariance of the elastic tensor must be satisfied [22]. Therefore, the elastic tensor can be written as

$$E_{ijkl} = \begin{bmatrix} E_{1111} & E_{1122} & E_{1133} & 0 & 0 & 0 \\ E_{1122} & E_{2222} & E_{2233} & 0 & 0 & 0 \\ E_{1133} & E_{2233} & E_{3333} & 0 & 0 & 0 \\ 0 & 0 & 0 & E_{2323} & 0 & 0 \\ 0 & 0 & 0 & 0 & E_{1313} & 0 \\ 0 & 0 & 0 & 0 & 0 & E_{1212} \end{bmatrix}. \tag{2.2}$$

It is typical to write the elastic matrix in contracted notation as the stiffness matrix C_{ij} with the stress strain relation in indicial notation

$$\sigma_i = C_{ij}\varepsilon_j \qquad i,j = 1,2,3,4,5,6. \tag{2.3}$$

And matrix notation

$$\begin{Bmatrix} \sigma_1 \\ \sigma_2 \\ \sigma_3 \\ \tau_{23} \\ \tau_{31} \\ \tau_{12} \end{Bmatrix} = \begin{bmatrix} C_{11} & C_{12} & C_{13} & 0 & 0 & 0 \\ C_{12} & C_{22} & C_{23} & 0 & 0 & 0 \\ C_{13} & C_{23} & C_{33} & 0 & 0 & 0 \\ 0 & 0 & 0 & C_{44} & 0 & 0 \\ 0 & 0 & 0 & 0 & C_{55} & 0 \\ 0 & 0 & 0 & 0 & 0 & C_{66} \end{bmatrix} \begin{Bmatrix} \varepsilon_1 \\ \varepsilon_2 \\ \varepsilon_3 \\ \gamma_{23} \\ \gamma_{31} \\ \gamma_{12} \end{Bmatrix}, \tag{2.4}$$

where C_{ij} are stiffness coefficients which are a combination of orthotropic elastic stiffness terms. In order to express the material constitutive equations with the engineering constants, Young's modulus, shear modulus and Poisson's ratio it is easier to write Hooke's Law with the compliance matrix, obtained by inverting the stiffness matrix [23].

$$\begin{Bmatrix} \varepsilon_1 \\ \varepsilon_2 \\ \varepsilon_3 \\ \gamma_{23} \\ \gamma_{31} \\ \gamma_{12} \end{Bmatrix} = \begin{bmatrix} S_{11} & S_{12} & S_{13} & 0 & 0 & 0 \\ S_{12} & S_{22} & S_{23} & 0 & 0 & 0 \\ S_{13} & S_{23} & S_{33} & 0 & 0 & 0 \\ 0 & 0 & 0 & S_{44} & 0 & 0 \\ 0 & 0 & 0 & 0 & S_{55} & 0 \\ 0 & 0 & 0 & 0 & 0 & S_{66} \end{bmatrix} \begin{Bmatrix} \sigma_1 \\ \sigma_2 \\ \sigma_3 \\ \tau_{23} \\ \tau_{31} \\ \tau_{12} \end{Bmatrix}. \tag{2.5}$$

Furthermore, it can be seen that for a unidirectional lamina there exists an infinite amount of symmetry planes about the 1-axis, making the material transversely isotropic. For this type of material, the following relations can be obtained for a material with fibers running in the 1-direction,

$$\begin{gathered} S_{11} = \frac{1}{E_1}, \qquad S_{22} = S_{33} = \frac{1}{E_2} = \frac{1}{E_3}, \qquad S_{55} = S_{66} = \frac{1}{G_{12}} = \frac{1}{G_{13}}, \\ S_{12} = S_{13} = \frac{-\nu_{21}}{E_2} = \frac{-\nu_{31}}{E_3}, \qquad S_{12} = S_{21} = \frac{-\nu_{21}}{E_2} = \frac{-\nu_{12}}{E_1}, \\ S_{23} = \frac{-\nu_{23}}{E_2}, \qquad S_{44} = 2(S_{22} - S_{23}) = \frac{1}{G_{23}} = \frac{2(1 + -\nu_{23})}{E_2}, \end{gathered} \tag{2.6}$$

reducing the number of independent non-zero constants to five engineering constants, to fully express the slots of the compliance matrix.

For most structural applications, composites can be assumed to be loaded in a plane stress state, considering that most parts are thin-walled structures [22]. Therefore, all the out-of-plane stress components (3-direction) are zero, leaving the in-plane compliance matrix:

$$\begin{Bmatrix} \varepsilon_1 \\ \varepsilon_2 \\ \gamma_{12} \end{Bmatrix} = \begin{bmatrix} S_{11} & S_{12} & 0 \\ S_{12} & S_{22} & 0 \\ 0 & 0 & S_{66} \end{bmatrix} \begin{Bmatrix} \sigma_1 \\ \sigma_2 \\ \tau_{12} \end{Bmatrix}. \tag{2.7}$$

And in terms of engineering constants in plane compliance is:

$$\begin{Bmatrix} \varepsilon_1 \\ \varepsilon_2 \\ \gamma_{12} \end{Bmatrix} = \begin{bmatrix} \frac{1}{E_1} & \frac{-\nu_{21}}{E_2} & 0 \\ \frac{-\nu_{12}}{E_1} & \frac{1}{E_2} & 0 \\ 0 & 0 & \frac{1}{G_{12}} \end{bmatrix} \begin{Bmatrix} \sigma_1 \\ \sigma_2 \\ \tau_{12} \end{Bmatrix}. \tag{2.8}$$

Finally, as can be seen from equation (2.8), leaving four independent non-zero constants have to be determined in order to fully characterize the elastic behavior of a fiber laminae. Note that the major Poisson's ratio ν_{12} and the minor Poisson's ratio ν_{21} can be determined by using the inverse relationship

$$\frac{-\nu_{12}}{E_1} = \frac{-\nu_{21}}{E_2}. \tag{2.9}$$

Therefore, the four material properties E_1, E_2, ν_{12} and G_{12} need to be determined in order to characterize the material as an input for the modeling and simulation. There are different ways to determine those properties. The vendor publishes data through datasheets that can be used. However, the material the FSAE team uses comes from

donations and has expired. Therefore, the properties possibly have been degraded and don't match the vendor data anymore. Additionally, the manufacturing process chosen is different which affects the properties of the laminate. The most accurate way is to get reliable properties is therefore physical testing.

2.1.2 Material Testing

Three different tests are necessary to characterize the four independent constants, two tensile tests and one in-plane shear test. The testing procedure for fiber reinforced polymer is standardized by the American Section of the International Association for Testing Materials (ASTM). Two different types of material were utilized in the chassis and need to be characterized. The first one being a M46J unidirectional fiber with a TC250 resin system that was mainly used because of its high stiffness properties. The second type is a AS4 fiber as an eight harness satin weave cloth in a TC250 resin system.

2.1.2.1 Tensile Tests

The specification for tensile tests of fiber composites is documented in [24]. The tensile test is used to determine the Young's modulus and the Poisson's ratio of the material. Two different layups are necessary to test Young's modulus in the fiber and the transverse direction. For each test, at least five specimens are used in order to get an average value for the results to account for manufacturing imperfections.

The panels were laid up and cured at 250 °F with vacuum pressure at 28 inHg. The amount of plies was chosen to reach the specified thickness of the specimen. Grip tabs need to be applied to the tensile test specimen to assure that the coupon doesn't fail under a combined stress state induced by the grips of the tensile test machine. The elastic properties however, can be accurately determined without bonding tabs on the specimen, as long as failure properties are not of interest. The cured panels were cut to the

specified width with a tile saw and VPG CEA-XX-250UT-120 biaxial strain gauges [25] were applied to measure axial and transverse strain following the instructions in [26]. An Instron servo-hydraulic universal test machine was used to perform the tensile tests. The ramp speed of the crosshead was set to *0.01 in/sec.* The applied load is tracked during the process and recorded via NI/LabView DAQ so it can be evaluated using a Matlab script that post processes the gathered data and calculates the elastic properties utilizing the equations given in [24] and [27]. The stress-strain curve for test number 1.2 is displayed in Figure 6. It can be seen that the stress-strain response for a specimen in tension in the fiber direction is very linear all the way until fracture, since carbon fiber is a brittle material with a low failure strain and almost no necking. The stress-strain curve can be used to calculate Young's modulus of the material by evaluating the slope of the curve. The equation of a linear curve fit is given in Figure 6, showing Young's modulus of the material to be $E_1 = 29.11$ Msi.

The same process was used to evaluate Young's modulus in the transverse direction.

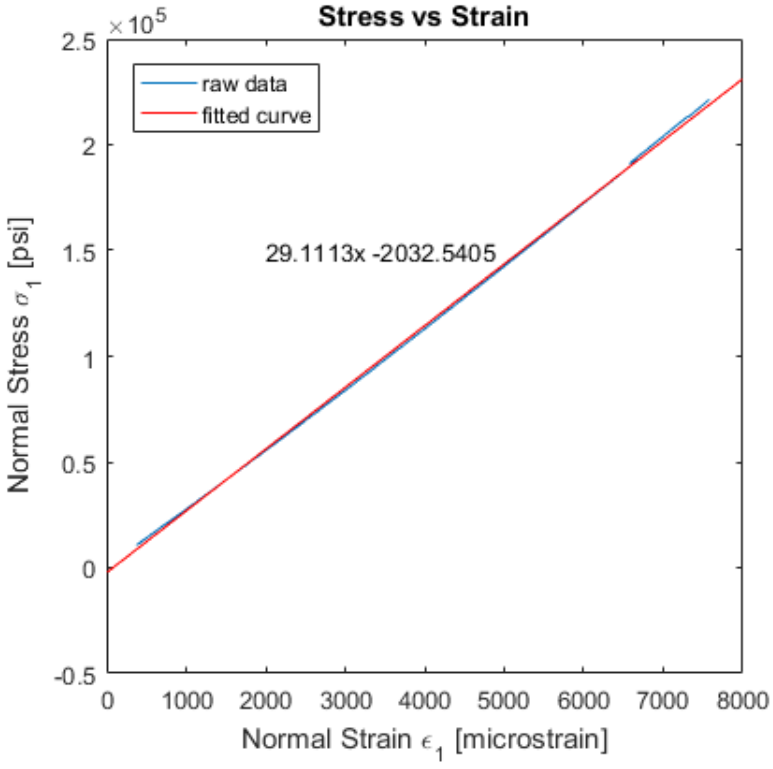

Figure 6: Stress-Strain curve for test number 1.2

Figure 7 shows the transverse strain over normal strain for test number 1.2. The slope can be used to evaluate the Poisson's ratio of the material. A linear curve fit was applied to the raw data and the equation evaluated resulting in a Poisson's ratio of $v_{12} = -0.22$. The slope is negative because the specimen compresses in the transverse direction when elongated axially, leading to a negative transverse strain. The definition for the major Poisson's ratio is given in [22] and includes a negative sign, giving

$$\nu_{12} = -\frac{\Delta\varepsilon_2}{\Delta\varepsilon_1} = 0.22. \tag{2.10}$$

It is worth noting that the transverse strain for AS4 is significantly lower due to the woven fiber that resists a compression in the transverse direction under tensile loads. The resulting Poisson's ratio is therefore much lower.

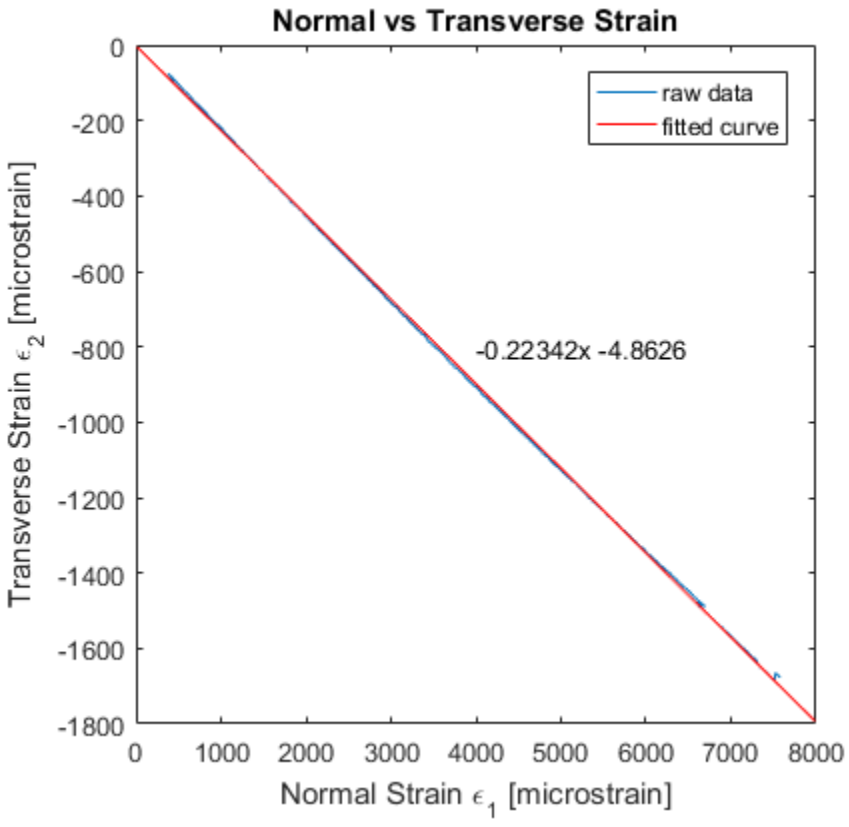

Figure 7: Normal Strain vs Transverse Strain curve for test number 1.2

The results for the fiber orientation test series of both M46J and AS4 are summarized in Table 1.

Table 1: Fiber direction tensile test specimen dimensions and results

Test #	Material	Layup	Thickness [in]	Width [in]	E_1 [Msi]	ν_{12}
1.1	M46J/TC250	$[0°]_6$	0.044	0.578	29.72	0.21
1.2	M46J/TC250	$[0°]_6$	0.046	0.529	29.11	0.22
1.3	M46J/TC250	$[0°]_6$	0.044	0.51	34.52	0.16
1.4	M46J/TC250	$[0°]_6$	0.045	0.651	24.24	0.25
1.5	M46J/TC250	$[0°]_6$	0.044	0.765	30.13	0.32
1.6	M46J/TC250	$[0°]_6$	0.043	0.583	27.63	0.14
1.7	M46J/TC250	$[0°]_6$	0.044	0.547	25.99	0.28
2.1	AS4/TC250	$[0°]_8$	0.13	0.9315	8.47	0.0007
2.2	AS4/TC250	$[0°]_8$	0.1305	0.9555	8.01	0.0092
2.3	AS4/TC250	$[0°]_8$	0.132	0.974	8.28	0.0025
2.4	AS4/TC250	$[0°]_8$	0.1325	0.9465	8.47	0.0015
2.5	AS4/TC250	$[0°]_8$	0.1305	0.9385	8.8	0.0009

The results for the transverse orientation test series of both M46J and AS4 are summarized in Table 2.

Table 2: Transverse direction tensile test specimen dimensions and results

Test #	Material	Layup	Thickness [in]	Width [in]	E_2 [Msi]
1.8	M46J/TC250	$[0°]_8$	0.0955	0.9405	-
1.9	M46J/TC250	$[0°]_8$	0.0935	0.9020	-
1.10	M46J/TC250	$[0°]_8$	0.0900	0.9140	0.75
1.11	M46J/TC250	$[0°]_8$	0.9200	0.9735	0.8
1.12	M46J/TC250	$[0°]_8$	0.0885	0.8820	0.81
1.13	M46J/TC250	$[0°]_8$	0.0920	0.8925	-
2.6	AS4/TC250	$[90°]_8$	0.132	0.947	8.03
2.7	AS4/TC250	$[90°]_8$	0.1345	0.9305	-
2.8	AS4/TC250	$[90°]_8$	0.132	0.9355	7.97
2.9	AS4/TC250	$[90°]_8$	0.131	0.923	8.41
2.10	AS4/TC250	$[90°]_8$	0.133	0.9445	8.21

The results that are missing in Table 2 were from specimen that broke in the grips of the test machine before load was applied. For future tests, it is recommended to use a larger amount of plies to get a thicker specimen in order to avoid them from breaking early.

2.1.2.2 In-Plane Shear Tensile Tests

The specification for in-plane shear tensile tests of fiber composites is documented in [27]. The in-plane shear test was used to determine the shear modulus of the material. Like the fiber and transverse direction tensile tests, five specimens were used and the test results averaged. The same cure cycle was used to cure the panels. Grip tabs are

not necessary for in-plane shear tests, since the tensile load is mostly carried by the resin instead of the fiber, which has significantly higher failure strains than carbon fiber. A higher ramp speed can be used in order to reduce the time necessary for the test. A speed of 0.06 in/s was chosen for all in-plane shear tests.

Figure 8 shows shear strain over shear stress for test number 1.14. It can be seen that the curve is non-linear, but with a linear region for low shear strain. Due to the angle of the fibers, the load is mostly carried by the resin, which has a viscoelastic material response. In order to calculate the shear modulus of the material, only the linear region is evaluated. [27] suggests to use shear strain ranging from approximately *1500 με* to *5500 με*. A curve fit has been applied to the linear region and the slope of its equation evaluated to get a shear modulus of $G_{12} = 0.49$ Msi.

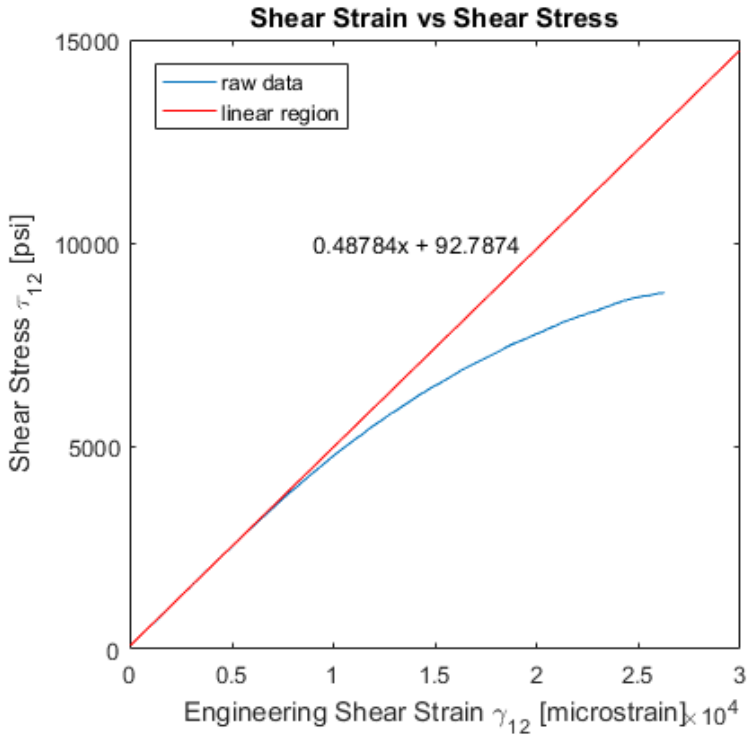

Figure 8: Shear Strain vs Shear Stress curve for test number 1.15

The results for the in-plane shear test series of both M46J and AS4 are summarized in Table 3.

Table 3: In-plane shear test specimens dimensions

Test #	Material	Layup	Thickness [in]	Width [in]	G_{12} [Msi]
1.14	M46J/TC250	$[\pm 45°]_8$	0.143	0.96	0.47
1.15	M46J/TC250	$[\pm 45°]_8$	0.143	0.87	0.49
1.16	M46J/TC250	$[\pm 45°]_8$	0.115	0.90	0.59
1.17	M46J/TC250	$[\pm 45°]_8$	0.156	0.91	0.45
1.18	M46J/TC250	$[\pm 45°]_8$	0.145	0.94	0.45
1.19	M46J/TC250	$[\pm 45°]_8$	0.138	0.96	0.42
2.11	AS4/TC250	$[\pm 45°]_4$	0.136	0.9505	0.55
2.12	AS4/TC250	$[\pm 45°]_4$	0.139	0.9325	0.52
2.13	AS4/TC250	$[\pm 45°]_4$	0.1385	0.9395	0.53
2.14	AS4/TC250	$[\pm 45°]_4$	0.136	0.9265	0.54
2.15	AS4/TC250	$[\pm 45°]_4$	0.1325	0.944	0.56

2.1.3 Composite Testing Results

The averaged ply thickness that has been gathered for the evaluation of the material properties and the averaged test results are summarized in Table 4. It can be seen that the values published by the vendor for the M46J Young's modulus in the fiber direction is 25 percent higher than the data tested. For the AS4, especially the shear modulus and Poisson's ratio are different than the vendor data, the least up to 40 percent. The discrepancy is partly due to manufacturing imperfections and the cure process. Because the specimens were cured without additional pressure besides the vacuum, the cured specimens ended up having a higher resin content and probably voids. Therefore, the fiber fraction volume is different which lowers the stiffness of the laminate. An indicator for the voids and high resin content is the measured ply thickness after the specimens were cured. The cured ply thickness under ideal conditions was calculated after [28],

$$cured\ ply\ thickness = \frac{fiber\ areal\ weight\ [\frac{lb}{in^2}]}{fiber\ volume\ fraction * fiber\ density\ [\frac{lb}{in^3}]}, \tag{2.11}$$

using the values given in the datasheet for the fiber density and fiber areal weight. The results are displayed in Table 4.

Table 4: Averaged material properties and comparison to vendor data

	M46J Tested	M46J Vendor	Percent Difference	AS4 Tested	AS4 Vendor	Percent Difference
Ply Thickness [in]	0.01149	0.0087	32.1	0.0167	0.0137	21.9
E_1 [Msi]	28.77	38.5	25.3	8.41	9.4	10.5
E_2 [Msi]	3.05	10	90.3	8.155	9.4	13.24
G_{12} [Msi]	0.48	0.57	15.8	0.54	0.77	29.9
v_{12}	0.267	0.27	1.1	0.003	0.005	40

The big difference in the shear properties could also be due to the resins age causing its properties to degrade. This can be seen especially with the E_2 test results, which are significantly lower than the vendor results.

However, this shows how important it is to characterize the material's constitutive response experimentally for accurate modeling. It also shows how the manufacturing process largely affects the outcome of the material response. The results from the material testing will be used as an input for the material database within Abaqus.

2.2 Aluminum Honeycomb Material Properties

Core is used in sandwich structures to separate the face-sheets (skins) to increase the effective bending stiffness. The idea is to have a light weight framework between the face-sheets that can carry the shear load for out-of-plane loading. The out-of-plane properties are therefore the most important ones to gather for the core. If the constitutive response of the core can be captured, it is not necessary to model the actual microstructure but replace it with a homogenous layer that has the same response instead [29].

Figure 9 shows a single cell of a honeycomb core, indicating the material directions as L and W direction. Due to the way of manufacturing, the walls in L-direction (1-direction or ribbon direction) are twice as thick as in the W-direction (2-direction). Therefore, the shear response for out-of-plane loading (3-direction) is different in the L-direction than in the W-direction, which means honeycomb core shows orthotropic behavior. As discussed in section 2.1.1 the elastic tensor for orthotropic materials consists of nine independent variables that can be expressed in engineering constants E_1, E_2, E_3, G_{12}, G_{23}, G_{13}, v_{12}, v_{23} and v_{13}, respectively.

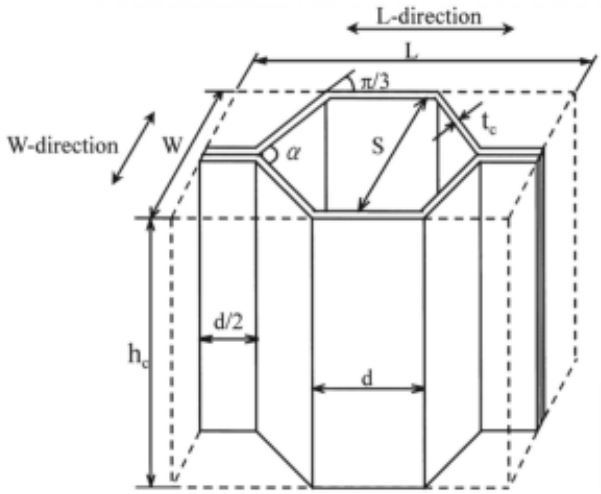

Figure 9: Single honeycomb cell [30]

The effective properties of the core can be found by either using analytical, numerical or experimental methods.

2.2.1 Honeycomb Properties - Experimental Method

Manufacturer of honeycomb sandwich material provide experimental data through publications like [31]. The standard test method for sandwich core is described in [32] along with some typical values. Those tests focus on the compressive (out-of-plane) properties E_3, G_{23} and G_{13} only.

Table 5: Engineering constants for the core from vendor [31]

Compressive modulus E_3 [psi]	Shear modulus G_{23} [psi]	Shear modulus G_{13} [psi]
74984.5	22045.7	44961.7

For the effective in-plane values, [31] suggests to use small numbers, close but not zero to avoid numerical problems, when modeling the core with homogenized properties. However, there are ways of determining those in-plane values in addition to the compressive properties given in the datasheet.

2.2.2 Honeycomb Properties – Analytical Method

Many closed form solutions have been found for the effective in-plane properties of cellular structures. Schwinghackl [33] is providing an overview of values for different theories and a comparison with experimental values. The in-plane values differ by order of magnitude of three for the shear modulus G_{12} and the two Young's modulus E_1 and E_2. The Poisson's ratios v_{12}, v_{23} and v_{13} reach values from 0 to 1.

In [34], an overview of mathematical models is given to calculate in-plane and out-of plane properties for honeycomb structures.

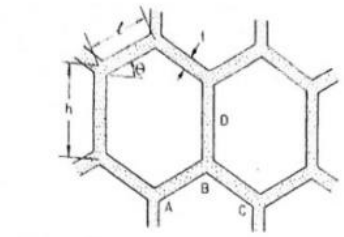

Figure 10: Geometry of the honeycomb structure [34]

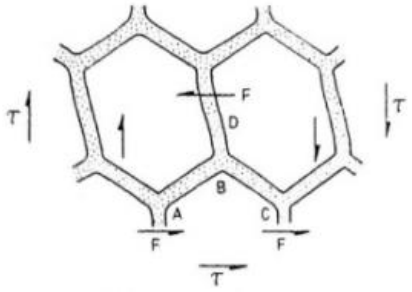

Figure 11: Deformation under in-plane shear load [34]

The equation for the in-plane shear modulus,

$$\frac{G_{12}}{E} = \left(\frac{t}{l}\right)^3 * \frac{\frac{h}{l} + \sin(\theta)}{\left(\frac{h}{l}\right)^2 \left(1 + 2\frac{h}{l}\right) * \cos(\theta)}, \tag{2.12}$$

with,

$$\theta = 60°, \quad \text{for regular hexagonal cells} \tag{2.13}$$

$$h = l = 0.1097 \text{ in}, \quad \text{and} \tag{2.14}$$

$$t = 0.001 \text{ in}, \tag{2.15}$$

can be used to calculate the effective shear modulus of the hexagonal cell core for a given cell size, Figure 10. The shear modulus G_{12} can be calculated to $G_{12} = 4.46$ *psi.*

[35] presents an early method on how to evaluate in-plane Poisson's ratio for various cell shapes. Hoffmann found that Poisson's ratio is a function of the wall angle Θ in Figure 10 only. Therefore, the in-plane Poisson's ratio v_{12} can be found from,

$$\nu_{12} = \cot(\theta)\,[\cot(\theta) + \csc(\theta)]. \tag{2.16}$$

Which results in $v_{12} = 1$ for a regular hexagonal cell with a wall angle of $\Theta = 60°$. He also found that large variations of the in-plane Poisson's ratio of the core has very little effect on a composite sandwich panel, as long as the bending stiffness of the core is well below the bending stiffness of the face sheet.

Newer studies utilize numerical methods in order to get more accurate effective properties of honeycomb structures, as they don't need to make a lot of simplifying assumptions.

2.2.3 Honeycomb Properties – Numerical Method

A very common method on finding effective properties of orthotropic materials is the "unit cell method". It utilizes the symmetry of the microstructure and Hooke's law in order to find the engineering constants, demonstrated in Figure 12. Penado [29] found that the unit cell can be further reduced to only 1/8 of a unit cell if the boundary conditions are studied carefully and applied correctly. He provides a list of boundary conditions for the determination of all necessary engineering constants, Figure 15.

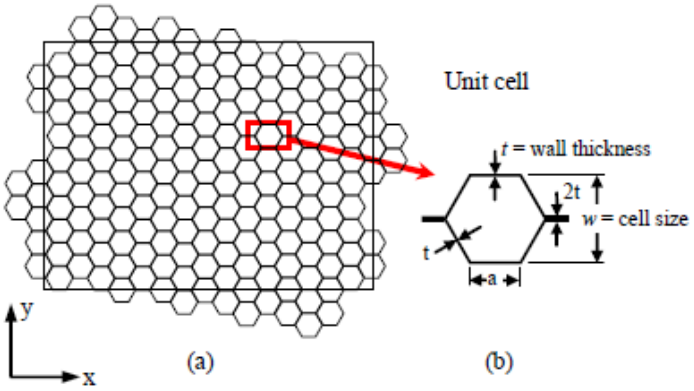

Figure 12: (a) Plan view of hexagonal cell core; (b) Unit cell [29]

The same modeling approach can be used for the regular hexagonal aluminum 5052 core with a cell size of *w = 0.1875 in* and a wall thickness of *t = 0.001 in*. The dimensions of the segment are determined by the cell size and its symmetry, Figure 13. The height *h* of the cell can be chosen arbitrary, since the amount of symmetry planes is infinite in that orientation. The dimensions for the model are summarized in Table 6.

Table 6: Cell segment dimensions

Cell height h/2 [in]	Wall width a/2 [in]	Wall thickness t [in]	Wall angle Θ [°]
0.1	0.05485	0.001	60

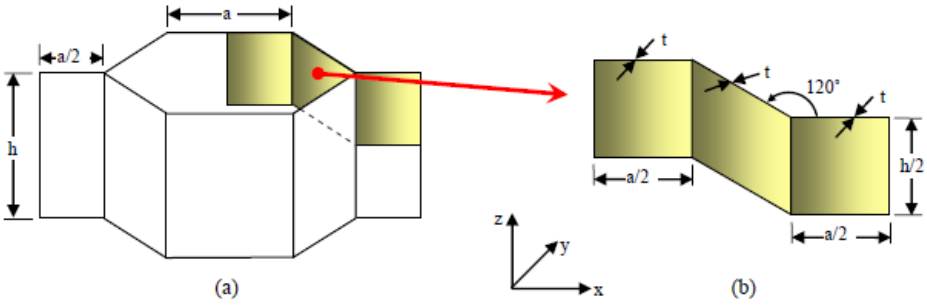

Figure 13: (a) 3-D view of unit cell; (b) 1/8 segment used for modeling [29]

Based on the findings of Penado [29], 4-node shell elements with full integration (S4) have been used to build the segment of a unit hexagonal cell. The symmetry of the model allows for a constant wall thickness. A displacement boundary condition is applied for all of the three directions, for higher stability of the model. The displacement is applied to a reference point that is rigidly connected to the face, so that the reaction forces can be evaluated on that point. The boundary conditions have been applied according to Figure 14.

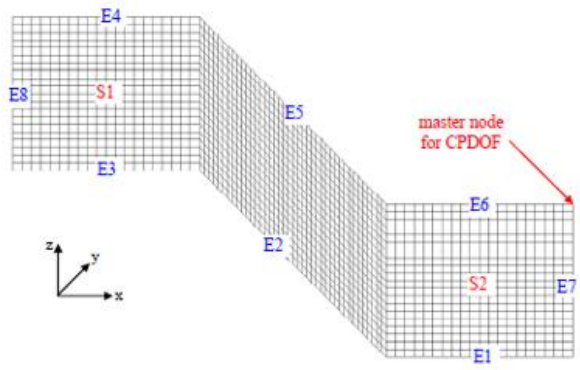

Figure 14: Labelled edges and surfaces for boundary conditions [29]

Location (see **Figure 3(b)**)	Boundary conditions†								
	E_x, ν_{xy} and ν_{xz}	E_y, ν_{yx} and ν_{yz}	E_z, ν_{zx} and ν_{zy}	G_{xy}	G_{yx}	G_{xz}	G_{zx}	G_{yz}	G_{zy}
E1	SZ	SZ	SZ	SZ	SZ	AZ	AZ	AZ	AZ
E2	SZ	SZ	SZ	SZ	SZ	AZ	AZ	AZ	AZ
E3	SZ	SZ	SZ	SZ	SZ	AZ	AZ	AZ	AZ
E4	u_z uniform (CPDOF)	u_z uniform (CPDOF)	$u_z = 1$	free	free	$u_x = u_y = 0$	$u_x = 1$ $u_y = u_z = 0$	$u_x = u_y = 0$	$u_y = 1$ $u_x = u_z = 0$
E5	u_z uniform (CPDOF)	u_z uniform (CPDOF)	$u_z = 1$	free	free	$u_x = u_y = 0$	u_x=1 $u_y = u_z = 0$	$u_x = u_y = 0$	$u_y = 1$ $u_x = u_z = 0$
E6	u_z uniform (CPDOF)	u_z uniform (CPDOF)	$u_z = 1$	free	free	$u_x = u_y = 0$	$u_x = 1$ $u_y = u_z = 0$	$u_x = u_y = 0$	$u_y = 1$ $u_x = u_z = 0$
E7	$u_x = 1$	u_x uniform (CPDOF)	u_x uniform (CPDOF)	$u_y = 1$	AX	$u_z = 1$ $u_x = u_y = 0$	AX	SX	SX
E8	SX	SX	SX	AX	AX	AX	AX	SX	SX
S1	SY	SY	SY	AY	AY	SY	SY	AY	AY
S2	u_y uniform (CPDOF) AR = 0	$u_y = -1$ AR = 0	u_y uniform (CPDOF) AR = 0	AY	$u_x = -1$ $u_y = u_z = 0$	SY	SY	$u_z = -1$ $u_x = u_y = 0$	AY

†SX, SY, SZ = symmetry conditions with respect to a plane perpendicular to the X, Y, Z axis; AX, AY, AZ = anti-symmetry conditions with respect to a plane perpendicular to the X, Y, Z axis; u_x, u_y, u_z = displacement in the x, y, z direction; CPDOF = coupled degrees of freedom; AR = all rotations.

Figure 15: Boundary Conditions for different loading cases based on [29]

The table in Figure 15 includes additional engineering constants G_{yx}, G_{zx} *and* G_{zy} that Penado used to validate the boundary conditions of the model. Those values were not calculated in the scope of this project since they are not necessary to characterize the materials constitutive response.

A convergence study was performed to find the necessary mesh size. The reaction force in x-direction has been plotted over the amount of degrees of freedom (DOF). A seed size of *0.005 in* has been found to be sufficient, giving a total number of degrees of freedom of *DOF = 16254* and a reaction force of $F_x = 2.63\ lb$, as can be seen in Figure 16. The size of this mesh has been used to execute simulations in all three directions.

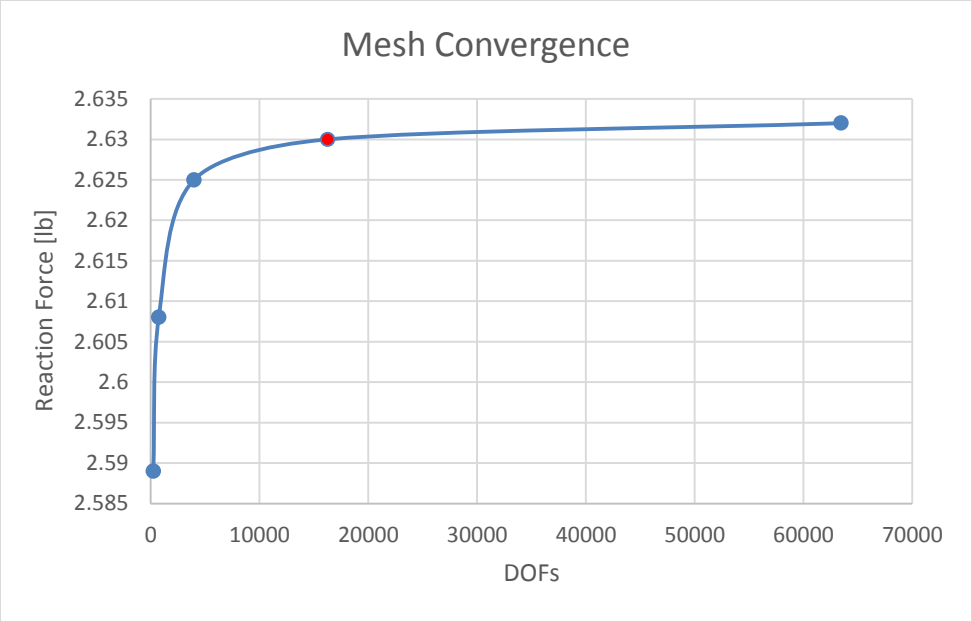

Figure 16: Mesh convergence study for the cell segment

Hooke's law can be solved for Young's modulus and calculated by evaluating the reaction force in the i-direction that is necessary to produce a unit displacement in the i-direction:

$$E_i = \frac{\sigma_i}{\varepsilon_i} = \frac{F_i L_i}{u_i A_i}. \tag{2.17}$$

Poisson's ratio can be calculated by evaluating the displacement in j-direction when a unit displacement is applied in the i-direction,

$$\nu_{ij} = -\frac{\varepsilon_j}{\varepsilon_i} = -\frac{u_j L_i}{u_i L_j}, \tag{2.18}$$

where *i, j = x, y, z* are the three directions in which the material is characterized.

The length L_i is the projected length of the cell in the i-direction and the area A_i is the projected area in the i-plane. The cell is treated as a block of solid material in terms of its dimensions.

Three studies have been executed for the three different directions of unit displacements $u_x = u_y = u_z = 1\ in$, and the reaction forces evaluated. Additionally, the displacements in for the unconstraint directions have been evaluated to calculate Poisson's ratio. The results are summarized in Table 7.

Table 7: Results for the effective material properties of the core

E_1 [psi]	E_2 [psi]	E_3 [psi]	v_{12}	v_{23}	v_{13}
89.62	46.80	166909.72	1.03	0.13	0.15

It can be seen that the in-plane Poisson's ratio $v_{12} = 1.03$ is very close to one which agrees with the closed form solution gathered in section 2.2.2. Young's modulus for the out-of-plane direction $E_3 = 166.91\ ksi$ is much higher than the compressive modulus $E_3 = 74.98\ ksi$ from the datasheet. This is due to the elastic buckling that happens in the thin walls of the cell, that the model is not accounting for.

2.2.4 Summary of the Honeycomb Properties

The results gathered from experimental, analytical and numerical methods are summarized in Table 8.

Table 8: Summary of calculated effective properties for the honeycomb core

E_1 [psi]	E_2 [psi]	E_3 [psi]	G_{12} [psi]	G_{23} [psi]	G_{13} [psi]	v_{12}	v_{23}	v_{13}
89.62	46.80	74984.5	4.46	22045.7	44961.7	1.0	0.13	0.15

It can be seen that the in-plane properties E_1, E_2 and G_{12} are very small and therefore insignificant for the overall structure.

The calculated values are used to calculate the compliance matrix for orthotropic materials as given in section 2.1.1, to check if the values are physically reasonable. Since the compliance matrix is symmetric, it also must be positive definite. A Matlab script can be used to calculate the compliance matrix and check if it is positive definite. When substituting the calculated values into the compliance matrix the result is a non-positive definite matrix, therefore the values need to be changed in order to be useful as an input to the model. The code was used to find the smallest values for E_1, E_2 and v_{12} in order to satisfy the restrictions given by the physical relevance of the compliance matrix for orthotropic materials. The engineering constants that satisfy the constraints of the compliance matrix are summarized in Table 9. Those values are used as an input for the model.

Table 9: Engineering constants that satisfy compliance matrix restrictions

E_1 [psi]	E_2 [psi]	E_3 [psi]	G_{12} [psi]	G_{23} [psi]	G_{13} [psi]	v_{12}	v_{23}	v_{13}
6000	2000	74984.5	4.46	22045.7	44961.7	0.9	0.13	0.15

3. COMPONENT SCALE VALIDATION OF THE MATERIAL PROPERTIES

To evaluate the material properties and the simulation method, a simple sandwich panel was manufactured and its elastic behavior studied in a three-point-bend test. A model of the panel, utilizing different element types was created and the results compared to the physical test.

3.1 Physical Test

A three-point-bend test is used to determine the flexural strength and modulus of the panel structure. The modulus can be used to study the elastic behavior of the panel under a bending load, which tests both the properties of the skin and the core. Due to its simple geometry the stiffness is only influenced by thickness, width and length of the panel. It is therefore a good indicator of a materials response rather than the response of the structure which can be used to validate the gathered material properties and to study different modeling strategies.

3.1.1 Panel Manufacturing

The panel is made from two carbon fiber skins, film adhesive and aluminum hexagonal cell core, Figure 17. The film adhesive is used to bond the core to the skin. Only M46J/TC250 was used for the skin, since the fiber modulus is significantly higher and therefore the driving factor for the skin stiffness. The layup chosen for the skin is [-45/0/45] with a nominal core thickness of $t = 0.7\ in$ of the 5052 aluminum core characterized in section 2.2.

The panel was cured in a single stage cure at a vacuum pressure of $p = 28$ inHg without additional external pressure in an autoclave. The same standard 250 °F cure cycle as for the test specimen manufacturing, section 2.1.2, was used to cure the panel.

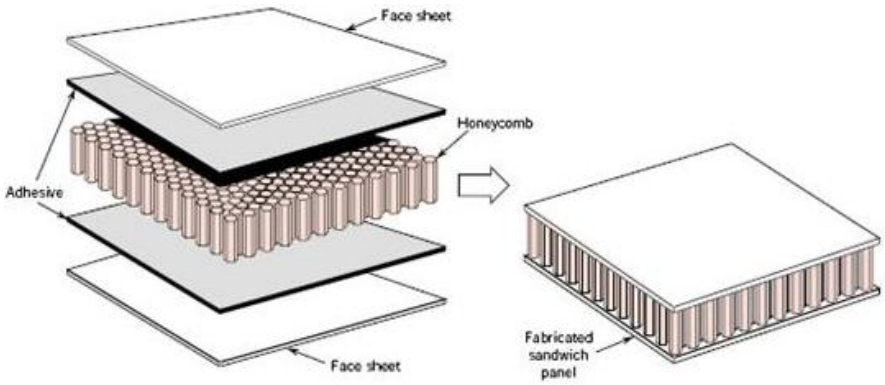

Figure 17: Structure of the sandwich panel

The dimensions of the panel were chosen to match the specifications of the official FSAE rules [1]. Therefore, the width of the panel must be *275 mm* and a length of a minimum of *500 mm*. The panel has been cut to the proper size on a tile saw.

3.1.2 Test Setup

The test is done on an Instron test machine, with a crosshead speed of *0.002 in/s*. The data acquisition was done with NI/LabView. The span and radius of the pin are specified by the official FSAE rules [1] and have been used for this test to get comparable data with tests that have been done in the past. The dimensions for the test setup can be seen in Figure 18. The span of the fixture must be *500 mm* long as defined by the rules [1], in order to provide a sufficient span to thickness ratio. The length of the panel must be bigger than the span to provide sufficient capability for the panel to slide when the bending load is applied. The radius of the pin is specified to be *50 mm*. A peak bending moment is created at the contact patch between the pin and the panel causing it to fail in that location.

The panel is simply supported by a welded steel fixture, Figure 19. A mark in the center of the panel has been used to accurately position the pin with respect to the panel.

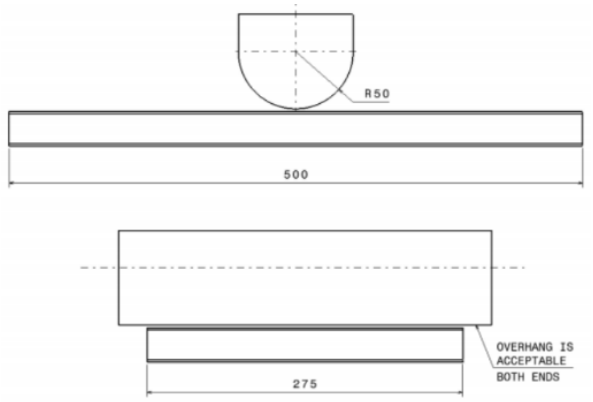

Figure 18: Three-point-bend test [1]

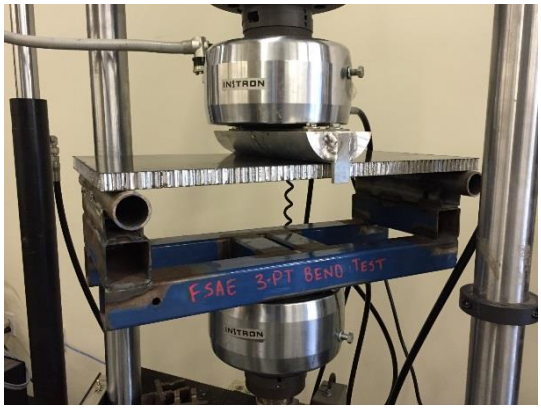

Figure 19: Test fixture

3.1.3 Component Test Validation

The load over displacement curve recorded during the test is displayed in Figure 20. The panel failed at a load of $F_{failure} = 972.6\ lb$ with a deflection of $\delta_{failure} = 0.265\ in$. The failed test panel can be seen in Figure 21. The panel failed due to local core crushing and fiber buckling. It can be seen that the dent in the center of the panel is deeper than on the edges which could be the result of curvature terms that result from the panel being in bending.

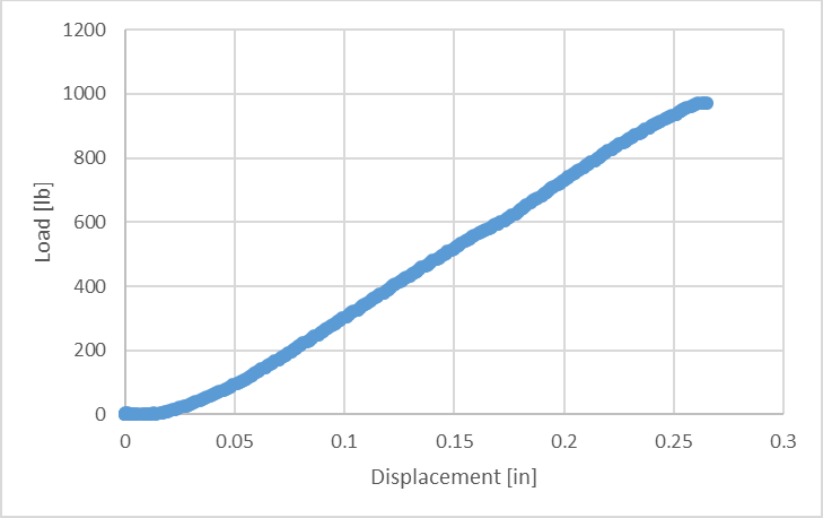

Figure 20: Load vs Displacement curve

Figure 21: Failed test panel

3.2 Simulation of the Component Test

3.2.1 Preliminary Sizing

The overall thickness of the panel has a large impact on the stiffness results of the model. It is a function of the thickness of each individual ply and the thickness of the core. The thickness of the physical panel has been measured before the test and its thickness

found to be $t_{total} = 0.725\ in$. A Matlab script that is compiling Classical Laminate Theory (CLT) and the equations for sandwich beam deflections as suggested in [31] was used to calculate the panel deflection for different core and ply thicknesses. The stiffness sensitivity for both the ply and core thickness have been plotted using the Matlab script, Figure 22 and Figure 23. Various combinations of ply thickness and core thickness are possible to reach the overall panel thickness, which have been examined in order to find the deflection value that matches the results from the physical test the closest. This way a core thickness of $t_{core} = 0.69\ in$ and a ply thickness of $t_{ply} = 0.0058\ in$ have been determined to give a maximum deflection of $\delta_{panel} = 0.248\ in$ under the measured failure load of the physical test of $F_{failure} = 972.6\ lb$. The nominal ply and core thickness differs from the thickness that has been found from the study. The measured panel thickness differs from the calculated panel thickness, respectively. Possible reasons for the fluctuation is the resin bleed into the cells of the core during the cure and the deformation of the core due to the vacuum pressure. The ply and core thickness that have been found giving the best results are used in the simulation.

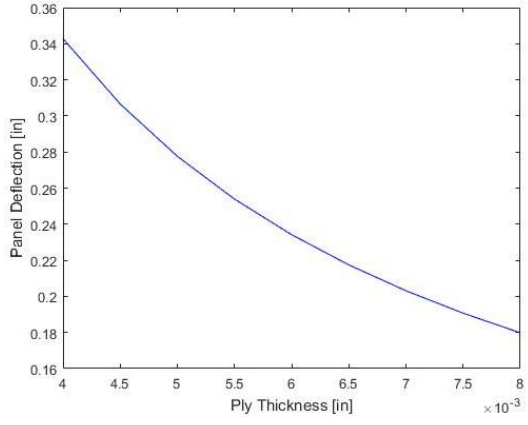

Figure 22: Stiffness sensitivity of the panel to ply thickness

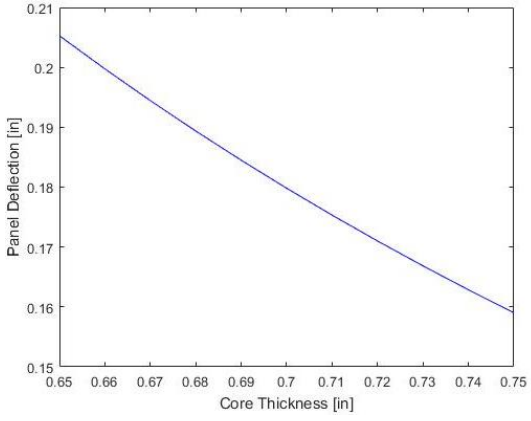

Figure 23: Stiffness sensitivity of the panel to core thickness

3.2.2 Component Modeling and Simulation

3.2.2.1 Pre-Processing

The pin is modelled as a rigid body to save computational time, since the deflection of the panel is much greater than the local deformation of the pin. The support structure is not modelled and instead replaced by boundary conditions, assuming them to be rigid as well. The support structure is made from steel and its local deflection therefore negligible with respect to the overall deflection of the panel. The dimensions have been chosen to match the test setup, compare section 3.1.2. The boundary conditions and modelled components can be seen in Figure 24.

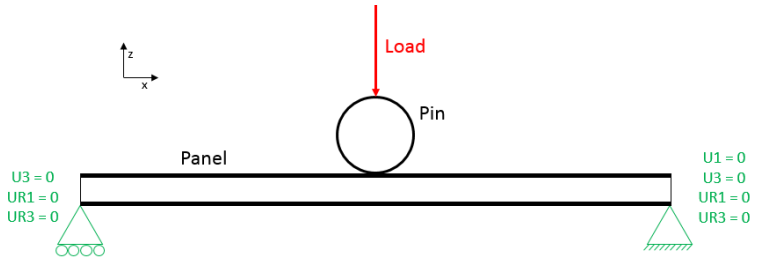

Figure 24: Component Simulation Boundary Conditions

The contact initiation between the pin and the top skin was defined as a frictionless, hard contact with a “surface-to-surface” contact formulation, to improve the representation of the curved surface of the pin, as suggested in [36]. Separation is allowed after contact initiation to allow for the larger deflection the edges that has been observed during the test. The load is applied as a concentrated force on the reference point of the rigid pin. Additionally, the rotational degrees of freedom and the in-plane movement of the pin are constraint, to prevent rigid body motion. The top and bottom skin are connected to the core utilizing a “surface-to-surface” tie constraint, which assumes a perfect bond and constrains all relative movement between the skin and the core. The analysis type was

chosen as a static, non-linear analysis due to the contact between the pin and the panel and the known load coming from the results of the physical test.

3.2.2.2 Element Choice and Mesh

The panel was modelled in three different ways utilizing different element types to work out how large their effect on the result is. The skin can be modelled using shell elements, since the thickness is small a plane stress state can therefore be assumed. Conventional shell elements with a quadratic formulation and reduced integration (S8R) were chosen, in order to capture the bending of the skin. The core's elastic compliance however is mainly through the thickness and must therefore be modelled with solid elements, that can capture the out-of-plane shear deflection. Hexahedral solid elements with a linear formulation and incompatible modes (C3D8I) were used. The seed size is adjusted to reach aspect ratios of one at the contact area. The element size for the skin is chosen larger than for the core, due to the master-slave formulation. Additionally, a larger element size is desired for the pin than the skin to prevent the rigid pin from penetrating the softer skin, as suggested in [37]. The mesh in the contact area can be seen in Figure 25.

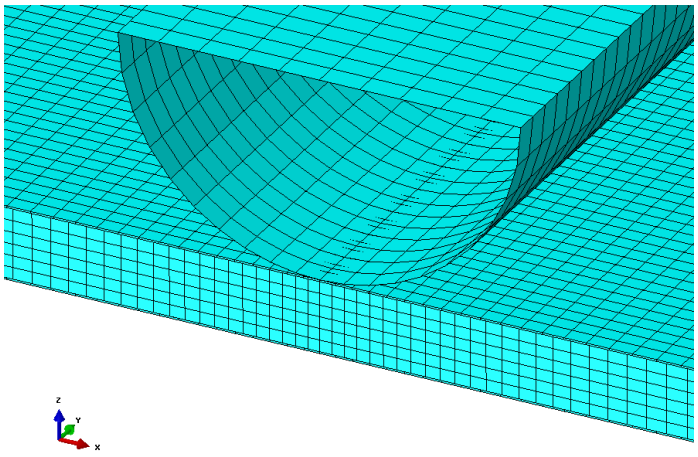

Figure 25: Mesh sizing in the contact area

Solid elements introduce a lot of degrees of freedom and therefore long computation times. For larger models it is desired to utilize simpler element formulations to keep the number of variables in the system to a minimum. Therefore, two additional models are developed modeling the panel as a single layer of shell elements including the properties of the core as a single ply within the composites pre-processor in order to study the impact on the results. The first model uses the same conventional shell elements that have been used for the skin with solid core elements, while the second one is using conventional shell elements with shear deformation. Those shell elements use a different formulation that allows to capture through-the-thickness stresses and strains, leading to a more stable out-of-plane contact initiation.

3.2.2.3 Post-Processing

An output request for the nodal displacement was created and processed within Abaqus. The resulting contour plot for the z-displacement of the model with solid elements for the core is given in Figure 26. The max deflection of the panel can be seen in the legend in the top left corner reading $\delta_{max} = -7.628\ mm$. Looking at the contour plot it can be seen that the maximum deflection occurs on the edges of the panel rather than in the center, which matches the observation made from examining the failed panel. Probing the amount of deflection of the reference point that is connected to the pin giving $\delta_{pin} = -6.65\ mm$. The pin deflection is the value measured during the test and is therefore used to compare results from the test with the simulation.

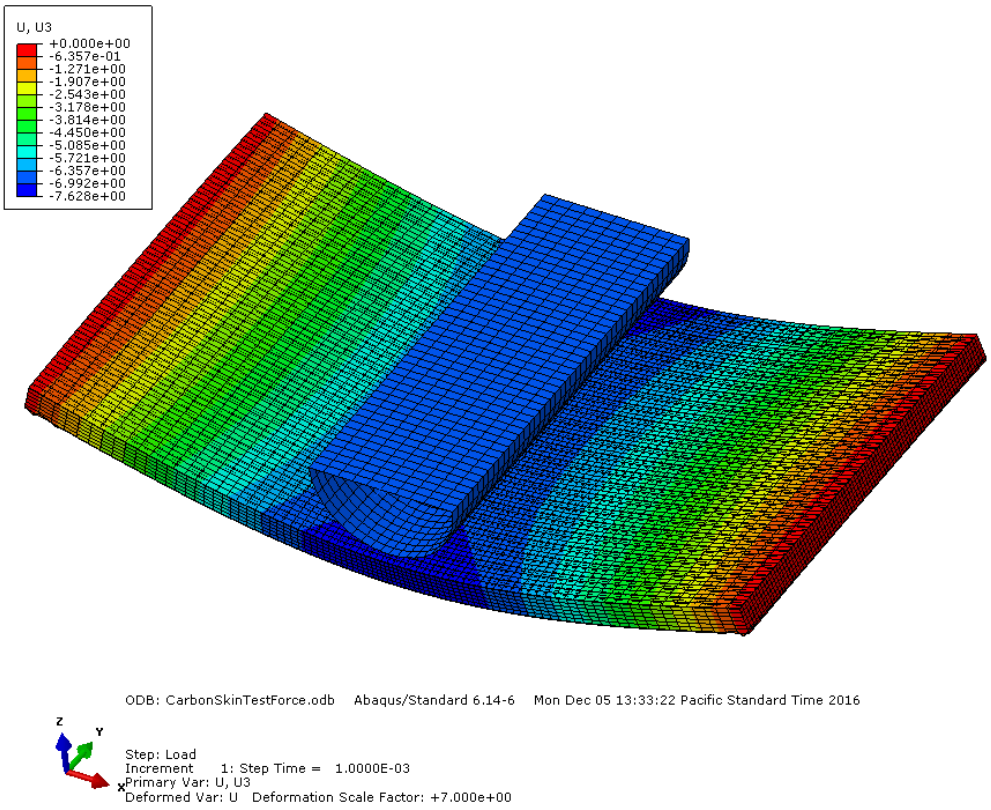

Figure 26: Z-Deflection of the panel with solid core elements

3.2.2.4 Modeling Issues Encountered

The contact between the conventional shell elements of the skin and the pin lead to convergence problems due to the formulation of the shell elements that can't capture through the thickness strains. Because of this, the contact was defined between the solid elements of the core and the pin in order to get stable convergence. The pin has also been offset to contact the core at contact initiation to remove the gap between the pin and the top surface of the core. It makes the post-processing easier too, since the offset doesn't have to subtracted from the final displacement.

Additionally, the boundary conditions needed to be defined at the edge of the core instead of the skin due to a conflicting master slave definition between the skin and the

core in order to ensure tie contact and boundary condition constraints between the edge of the skin and the core.

The model utilizing conventional shell elements for the panel encountered convergence problems leading to a long computation time and local penetration of the panel as a result, Figure 27. Adjusting time step size and contact stabilization were used to reach convergence, but the results still show local penetration, which is most likely a result of the poor out-of-plane contact formulation of the conventional shell elements.

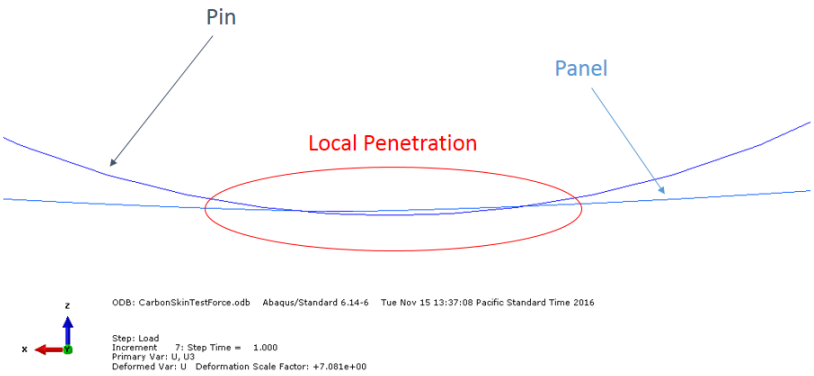

Figure 27: Local penetration of the panel in a center plane cut view

3.3 Results and Conclusion

The results from all three studies and the results from the CLT script are summarized in Table 10. A percentage error between the deflection results of the simulation and the test is given in the far right column to compare and quantify the different methods. The values are given in SI and imperial units because the simulation was performed using SI units due to the panel dimensions specified by the FSAE rules being in SI units.

Table 10: Results of the three-point-bend test models

	Load [lb]	Deflection [in]	Load [N]	Deflection [mm]	Percentage Error

Test	972.6	0.265	4326.3	6.73	-
CLT	972.6	0.248			- 6.41
FEA (solid)			4326.3	6.65	- 1.20
FEA (conv. shell)			4326.3	6.72	- 0.163
FEA (w/ shear deformation)			4326.3	6.66	- 1.06

The results from the simulation were within two percent, matching the results from the physical test very well. The deflection calculated using CLT results in a deviation from the experiment of less than 10 percent and is therefore a good method for preliminary sizing and to study sensitivities of the model due to the high flexibility of the code to implement changes and run through a lot of loops in a short amount of time.

It can be seen that the results from the simulation using solid elements to model the core and only shell elements only lead to a small deviation of about one percent. The difference between the model using conventional shell elements with shear deformation only and the model using solid elements is insignificantly small, with less than one percent. The biggest deflection was calculated by the model using the normal conventional shell elements

It seems surprising that the model utilizing conventional shell elements resulted in a bigger deflection, since it is not tracking the out-of-plane strains. However, taking a closer look at the contour plot, the bigger deflection is a result of contact problem of the simulation as mentioned in section 3.2.2.4. Conventional shell elements without the shear deformation shouldn't be utilized for problems that include through the thickness strains.

Since the shell element model has significantly less degrees of freedom and is also simpler to set up but resulting in almost similar results, the decision was made to model the sandwich structure using the conventional shell elements with shear deformation.

4. CHASSIS TORSIONAL STIFFNESS MODEL

After determining the constitutive response of the material and a modeling strategy for the sandwich structure of the monocoque part of the chassis have been found, the geometry of the chassis was modelled in Abaqus. The results from the simulation were then compared to the torsional test to determine how accurate the results of the simulation are and if further adjustments are needed in order to gain valid results.

4.1 Chassis Torsional Test

Before starting the modeling process, a torsion test of the chassis was executed in order to find its torsional stiffness. The stiffness result from the test is used as a baseline value to validate the model after the simulation process.

4.1.1 Test Setup

The fixture developed in 2014 to test the chassis' torsional stiffness was used to measure the 2016 chassis, Figure 28. The fixture consists of two steel I-beams (1), one in the front and one in the rear, that stiffen up the fixture to not distort the results of the test. For the test, all four wheels were removed from the car, and all four shocks of the car were replaced with steel bars (2), in order to eliminate displacement from the soft springs. Two adapter plates in the rear (3) bolt to the hubs to constrain all available degrees of freedom expect the rotation about that axle. Those adapter plates bolt to the rear I-beam. The front right upright of the chassis is simply supported by a pivot (4) that prevents the chassis from moving down. The front left suspension was unsupported and free to move up and down. Weights suspended from the front left hub (5) were used to load up the chassis. The deflection was measured with a gauge at the front left upright

(6), Figure 29. To prevent rotation of the front uprights, the rotation of the steering column was locked.

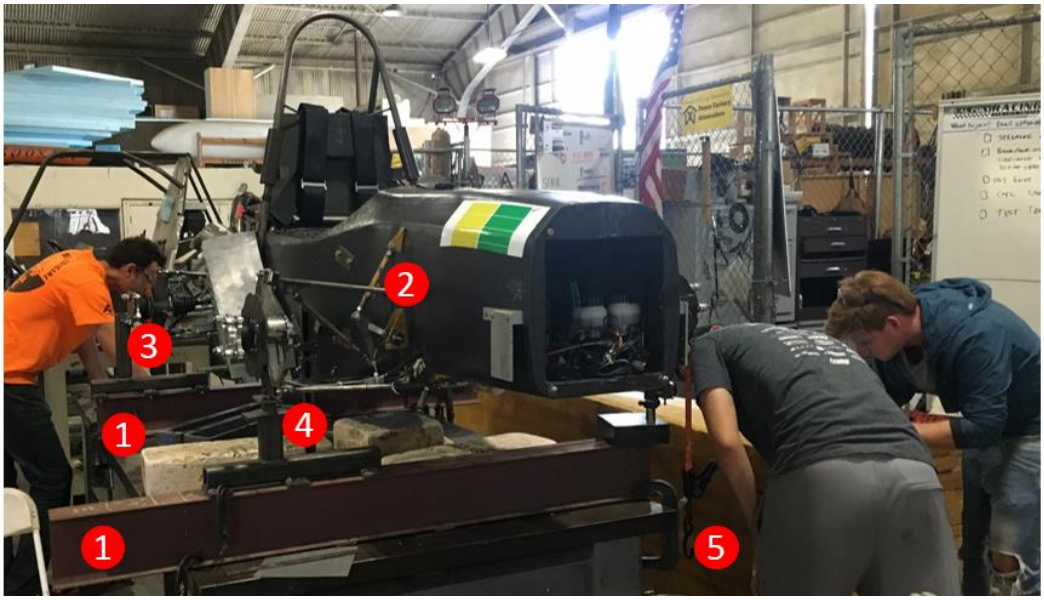

Figure 28: 2016 chassis on the torsional test fixture

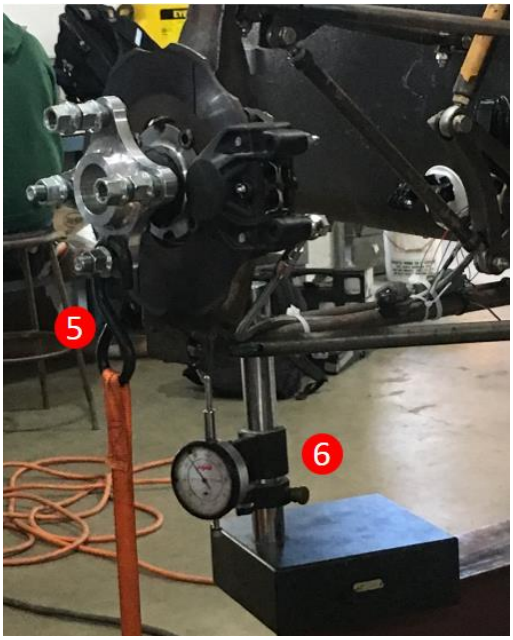

Figure 29: Gauge to measure the deflection at the front left upright

4.1.2 Torsion Test Process

After the chassis has settled in, the displacement gauge was zeroed. Weights were added to a bucket that was suspended from the upright and the deflection was measured and listed for each weight that is added to the bucket. The maximum weight was *107 lb*. After the maximum load is reached, the weights were removed one by one and the deflection was measured at each step, respectively. After the unloading was completed, the gauge was zeroed again so the next run can be executed. Due to the friction in the bearings, the deflection before loading and after unloading was different. Therefore, a test run is done to assure that bearings were settled in before measurements are taken. Three measured runs were done after that and the results averaged.

4.1.3 Torsion Test Results

The applied load and the distance from the pivot point at the front right upright $d_{moment} = 47.25$ in was used to calculate the applied torque. The deflection at the upright and the distance from the pivot point at the front right upright $d_{twist} = 43.75$ in was used to calculate the angle of twist of the chassis. Utilizing both results, the torsional stiffness of the chassis was calculated. The average torsional stiffness over three runs can be plotted as a function of the applied torque (Figure 30). It can be seen that a significant difference in torsional stiffness exists between loading and unloading. The observed hysteresis is due to the friction in the spherical bearings and rod ends in the suspension. The bearings settle in when the load on the chassis builds up but due to the friction the bearings stay in their deflected state during unloading. The measured deflection doesn't go back to zero after unloading because the friction in the bearings prevents a full rebound. The leftover deflection can be taken as an indicator for the deflection in the bearings. Two torsional stiffness tests have been done for both the electric car frame and the combustion car frame. The average leftover deflection for both tests was measured to

$\delta_{bearing} = 0.02445\ in$. It is an approximate bearing compliance that needs to be taken into account for the simulation. For the validation of the torsional stiffness model, the load-case associated with the point second to last in Figure 30 was chosen. The applied load at this point was $F = 100.987\ lb_f$, resulting an applied torque of $T = 397.64\ ft\text{-}lb$ and an average torsional stiffness of $k_t = 1308.29\ ft\text{-}lb/deg$.

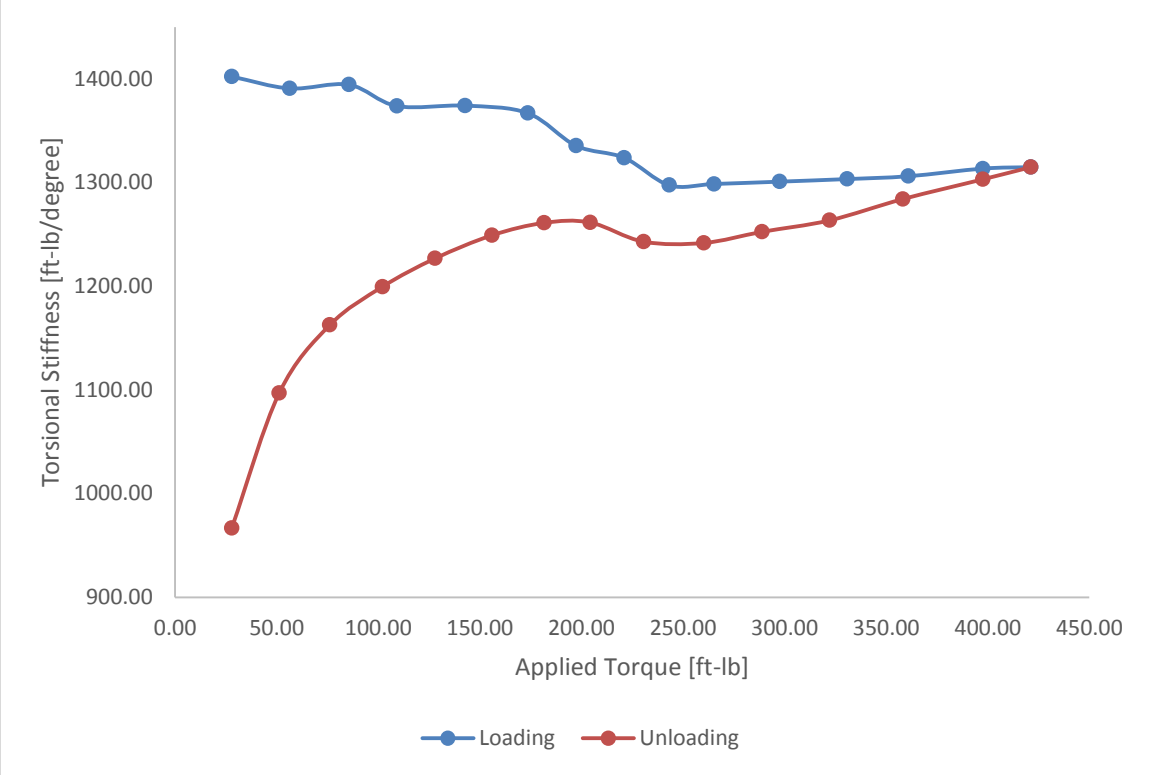

Figure 30: Average applied torque vs torsional stiffness curve

4.2 Modeling and Simulation

The components that affect the torsional stiffness of the chassis must be identified and modelled in a way that represents their stiffness with the least amount of computational time necessary.

4.2.1 Geometry

The main geometry of the chassis consisted of the four corners of the suspension, the carbon fiber reinforced polymer sandwich structure monocoque and the tubular steel spaceframe. Additionally, stiffening members like the front roll hoop and the engine, that act as parallel springs to the main structure, must be taken into account as they affect the overall torsional stiffness.

4.2.1.1 Monocoque

The design of the Monocoque is broken up into different areas specified by the FSAE rules. Those areas must meet certain strength requirements and end up with different laminates, respectively [1]. An overview of the different sections and the geometry of the 2016 monocoque is given in Figure 31. The layup of each section is given in Table 11. For each area a different composite layup must be defined within Abaqus.

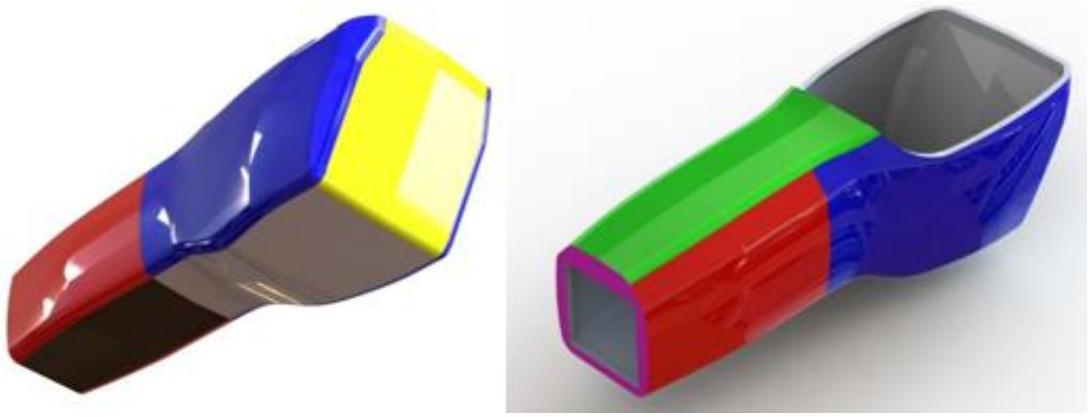

Figure 31: Layup sections of the monocoque [38]

Table 11: Overview of the layup sections

Color	Section	Layup[1]
	Side Impact Structure (SIS)	[0c / 45 / 0 / -45/ -45 / 0 / 45 / core]$_s$
	Front Bulkhead Support (FBHS)	[0c / 0 / -45 / 45 / core]$_s$
	Front Hoop Bracing (FHB)	[0c / 0 / -45 / 45 / core]$_s$
	Cockpit Floor (CF)	[0c / 0 / -45 / 45 / core]$_s$
	Front Floor (FF)	[0c / 0 / -45 / 45 / core]$_s$
	Seat back (SB)	[0c / 45 / 0 / -45/ -45 / 0 / 45 / core]$_s$
	Front Bulkhead (FBH)	[$(0c)_{10}$ / core]$_s$

As discussed in section 3.3 the sandwich structure which the monocoque is made of, can be modelled using shell elements. The geometry was imported from CAD as a surface geometry. The geometry was then split up into the sections mentioned above and assigned their proper composite layup. The bulkhead doesn't contribute to the torsional stiffness as only the structure between the suspension attachment points matter. Therefore, it was removed to simplify the mesh development.

4.2.1.2 Tubular Spaceframe

The spaceframe mainly consists of round profile tubes that are welded together. The only exception are the rectangular profiles that are used as bracings for the engine mounts. Similar to the monocoque, the diameter and wall thickness for most of the tubes is given by the FSAE rules [1]. An overview of the different tubing profiles for the 2016 combustion car spaceframe is given in Figure 32. The diameter and wall thickness of each profile is given in Table 12.

[1] The subscript 'c' after the ply angle indicates that the material is cloth (AS4)

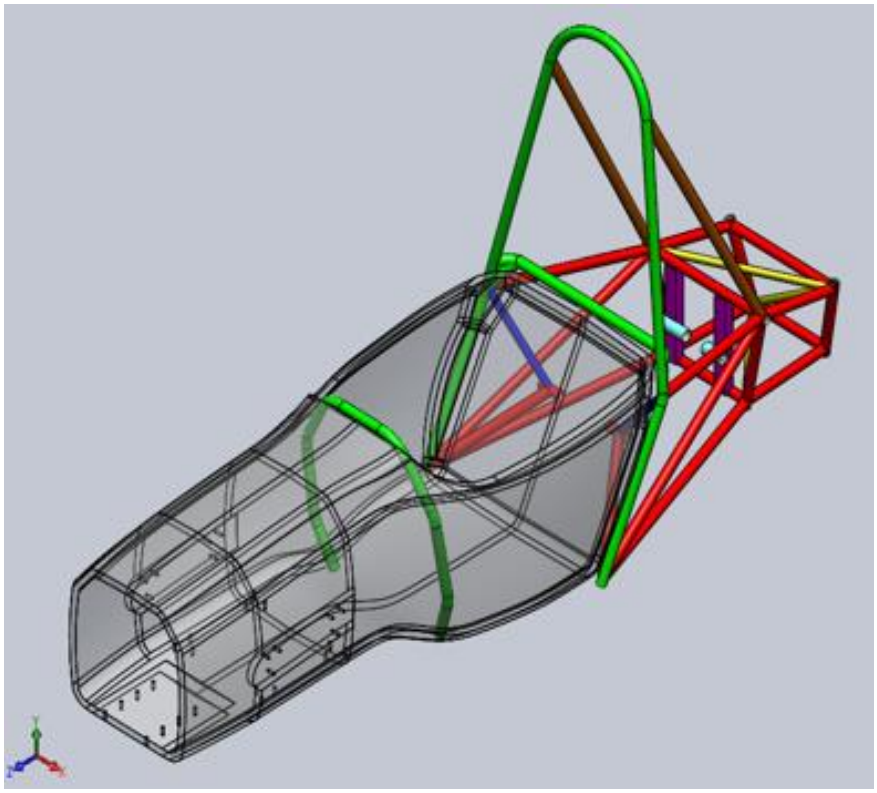

Figure 32: Tubing profiles of the rear spaceframe and roll hoop [38]

Table 12: Profile cross section overview

Color	Profile	Diameter [in]	Width [in]	Height [in]	Wall Thickness [in]
	Round	1	-	-	0.095
	Round	1	-	-	0.049
	Round	1	-	-	0.065
	Round	0.5	-	-	0.049
	Round	0.75	-	-	0.049
	Rectangular	-	2	1	0.065
	Round	1.25	-	-	0.049

Common practice is to model the spaceframe with beam elements of constant cross-section. In [2] the authors state that the Cornell FSAE team got good results using beam elements to represent the frame. The spaceframe is therefore imported as a wire model from CAD. Additionally, the front roll hoop is important as a wire frame model and placed within the monocoque. The proper cross sections must be assigned to the frame and the correct beam orientation must be found for the rectangular profile section. It is important to make sure that all nodes in the frame are properly connected after the import. Tie constraints were used to tie nodes together that weren't automatically connected after the import.

4.2.1.3 Suspension

Like the spaceframe, the suspension mainly consists of tubular profile sections that can be modelled as beam elements. Exceptions to this case are upright and rocker that are made from a welded box structure. A bottom-up modeling approach was used in order to represent those components in the global model.

The individual components need to be modelled in detail to find their effective stiffness. To avoid large computational times of the global chassis stiffness model, the detailed modeling of those components was done separately and the results interpreted within the global model. Beam elements with a cross section that results in an equivalent stiffness to the loading case in question were used in the global model of the chassis to represent uprights and rockers. In order to find the equivalent stiffness, a beam model of the individual component was subjected to the same loading case as the detailed 3-D model. By changing the cross section of the profile of the beam section profile, the same deflection and therefore the same stiffness was found. Once the cross section profile was found, the same section profile was used for the beam elements within the global model to represent the actual geometry.

Table 13 provides an overview of the cross sections that were used for the profiles of the suspension components. The points that the define the kinematics of the suspension were imported from a global variables text file and the points connected by wires within Abaqus. Each individual component needs to be an individual part, so that the kinematics of the system can be defined appropriately.

Table 13: Overview of profile sections for the suspension

Component	Profile	Diameter [in]	Wall thickness [in]
Upright	Pipe	1.134	0.03
Front Rocker	Circular	0.125	-
Rear Rocker	Circular	0.138	-
Lower Control Arm	Pipe	0.625	0.035
Upper Control Arm	Pipe	0.5	0.035
Shock	Pipe	0.5	0.035
Steer Link	Pipe	0.5	0.035
Push Rod	Pipe	0.5	0.035
Pull Rod	Pipe	0.5	0.035

4.2.1.4 Engine

The engine was modelled in different ways. One option was to model it as a block using solid elements, and the other was to model it as a surface body using shell elements. Either way, the geometry is not the driving factor for the stiffness of the engine. In its simplest way, the engine can be represented as a rigid body, since compared to all the other components in the main structure, its stiffness is orders of magnitude higher. Therefore, the modeling method shouldn't have too big of an effect on the overall stiffness as long as the model representing the engine is stiff enough. A surface model was

chosen to decrease computational time, respectively. The wall thickness of the engine was chosen so that the mass properties match the real engine.

The final assembly of the chassis model is displayed in Figure 33.

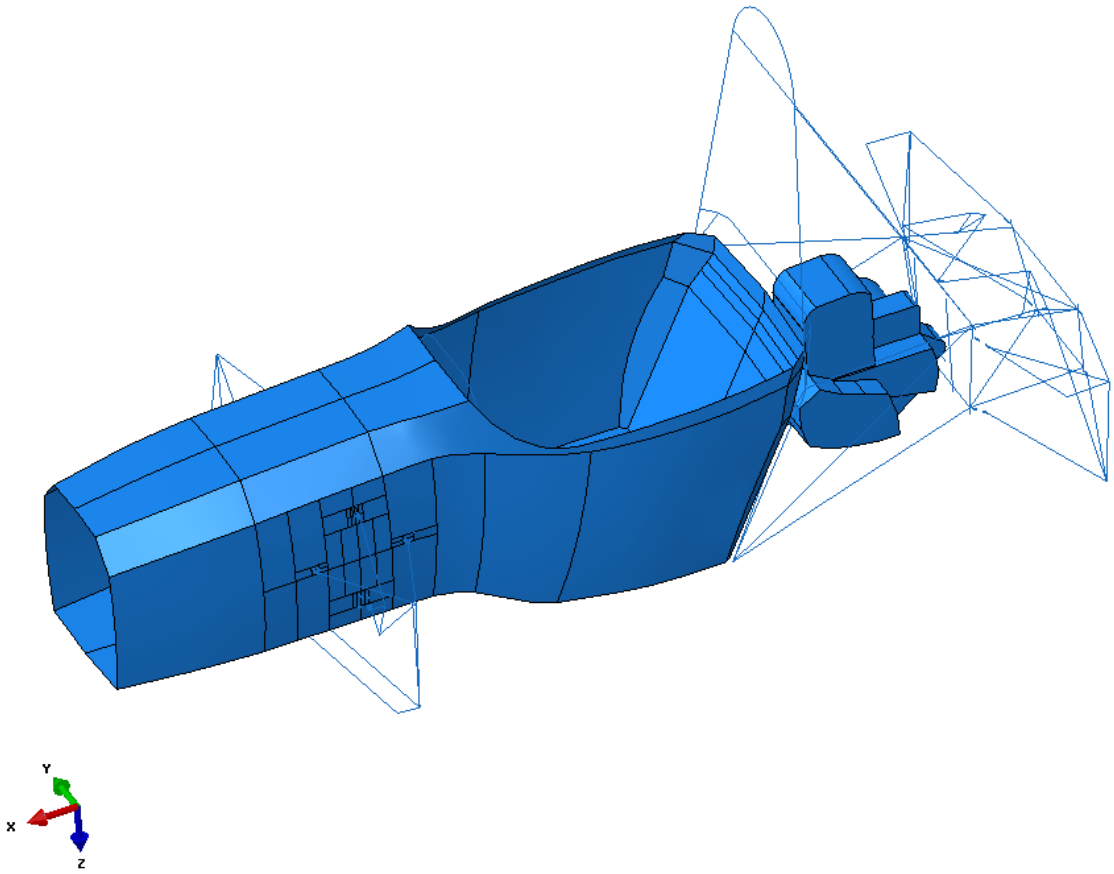

Figure 33: Final chassis model within Abaqus

4.2.2 Mesh and Element Choice

A mesh convergence was executed for the monocoque individually keeping the seed size of all other components the same. A plot for the z-deflection at the front left upright over the number of degrees of freedom can be seen in Figure 34. A global seed size of 0.5 in was found to be sufficient giving a number of DOF of 16112, see red marker in Figure 34. Conventional shell elements with shear deformation, eight nodes and quadratic formulation with reduced integration (S8R) were used to model the monocoque in order to capture the out-of-plane loads from suspension attachments. The average element aspect ratio is 1.19 with the worst element having an aspect ratio of 3.06 located at the seatback of monocoque. Only quadratic elements have been used for the mesh. The stacking direction for the shell elements was defined so that the surface model represents the outside skin.

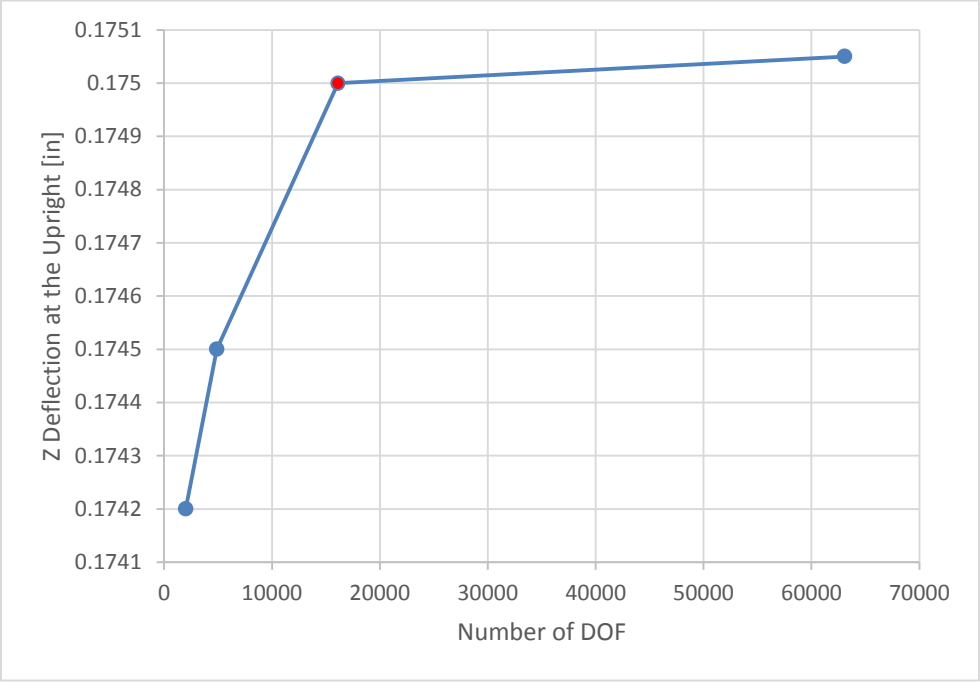

Figure 34: Mesh convergence plot for the monocoque

Next, a mesh convergence for the spaceframe was performed, keeping the seed size for all other components the same. Again, the z-deflection was probed at the front left upright and plotted over the number of DOF, as can be seen in Figure 35. A global seed size of 0.5 was found to be sufficient giving a number of DOF of 2548, see red marker in Figure 35. The seed size in areas of high curvature, was driven by the allowable radius of the beam elements. Linear beam elements with two nodes (B31) with shear capture were used to capture bending. Although the frame is triangulated and therefore not subjected to bending, rocker mounts, engine mounts and the mounts attaching the spaceframe to the monocoque are mostly between nodes and therefore introduce a bending moment into the frame.

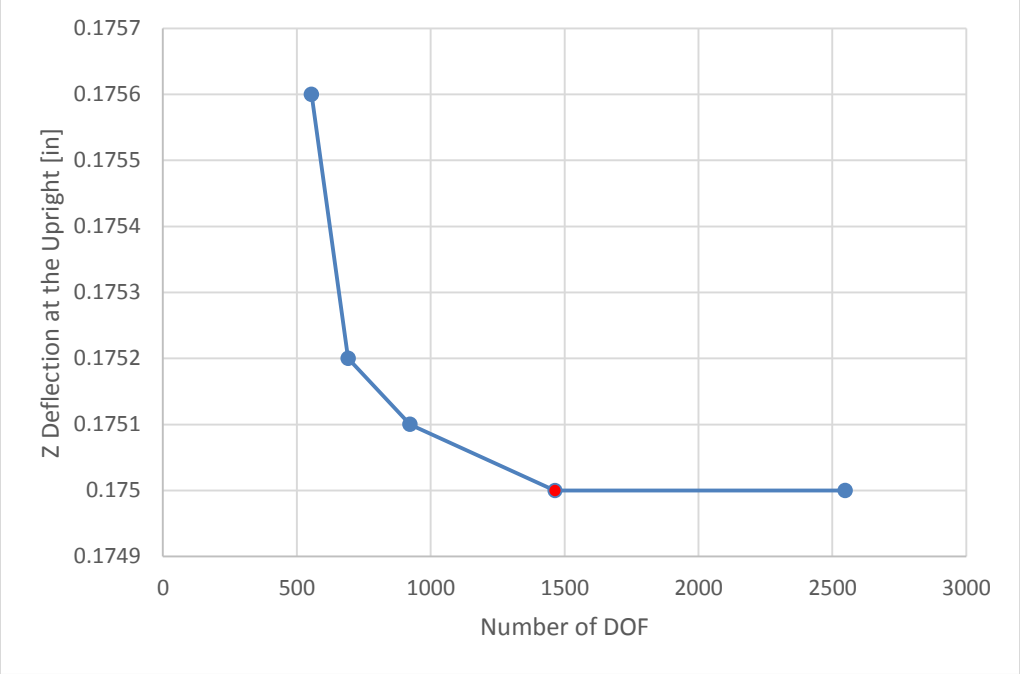

Figure 35: Mesh convergence plot for the spaceframe

The suspension components could technically be modelled with truss elements since they are two force components and therefore don't need to capture bending. However, using beam elements uncovers bending and shear and were therefore used instead to be able to check if the connections work accurately. The same element type as for the spaceframe has been used to model all suspension components. The seed size for most suspension components was chosen to 0.5, only the rockers and uprights have been meshed with a seed size of 0.1 to accurately capture the bending.

4.2.3 Connector Elements and Constraints

In order to accurately represent the kinematics of the suspension, the links must be modelled as two-force members, meaning them being subjected only to tension and compression forces. Therefore, the connection between the control arms, steer links and push/pull rods must be free of rotational constraints. Abaqus offers a special type of element, namely connector elements [37], that can be used to model such connections. Connector elements can be designed to allow individual degrees of freedom, allowing rotation about a single axis while all additional degrees of freedom are constrained, which has been used to define the connection between the rocker and the rocker mount. A coordinate system must be defined in order to assure the open rotation happens about the correct axis, especially of the rotation axis is lying in a tilted plane with respect to the global coordinate system and planes.

Connections between the front roll hoop, the spaceframe and the monocoque as well as welded joints such as the engine mounts have been modelled as tie constraints. It is important to control the influence area of those tie constraints. Partitions on the spaceframe and the monocoque have been used to create areas for the tie constraints and connector elements that represent the size of the mounts on the real chassis.

4.2.4 Boundary Conditions and Analysis Type

The boundary conditions were chosen to represent the torsion test. The rear uprights were constrained at the center node allowing only the rotation about the rear axis (UR2). The bottom node of the front right upright was constrained only in the z-direction (U3). A load of $F = 100.987\ lb_f$ was applied to the center node of the front right upright, representing the loading case from the physical test. The model including all the boundary conditions can be seen in Figure 36.

A static linear analysis was chosen to solve the model, due to small deflections and the absence of contacts or material non-linearities.

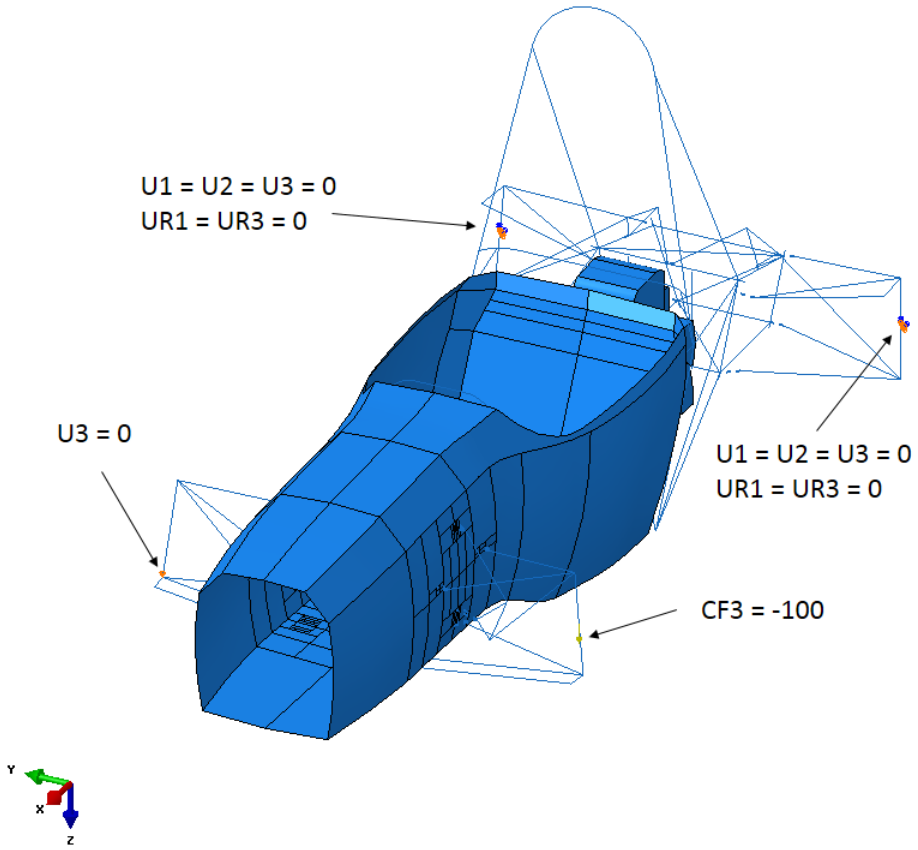

Figure 36: Boundary conditions of the chassis model

4.2.5 Modeling Issues Encountered

By far, the biggest difficulty was the proper definition of connections and constraints. Early on, an output request for section forces and moments was created in order to plot moments of the suspension members as a check to make sure the rotation-free connections work accordingly. The connector elements work best between two nodes that are coincident. Therefore, reference points were created, coincident with the nodes on the control arms and the rocker pivot. Those reference points were used to define the connection between the mount and the suspension component. The reference point was then connected to the monocoque with an additional connector element, that constraints all degrees of freedom, representing the mount from the monocoque to the suspension. If the mount stiffness is known, the elasticity for the six degrees of freedom can be defined within the connector element. Since mount stiffness' were not known, they were assumed rigid.

Grounding issues were encountered frequently, when connections overdefined the problem, leading to errors within the connector elements. Those errors lead to convergence problems and distorted results. High deformation scale factors can be used to visualize corrupted connections as they can be seen by excessive deflections. The definition of accurate coordinate systems to define rotation axis is crucial, in order to avoid overdefining the problem.

When switching between rigid and deformable body definitions, connector elements are more stable than constraints since they don't rely on master-slave relations. Their behavior was also not dependent on mesh size, while for constraints, the slave surface needs to be more refined than the master. The use of connector elements makes the model more flexible to changes which can be important when studying the behavior of the system to changes.

4.2.6 Chassis Torsion Simulation Results

In order to calculate the torsional stiffness of the chassis from the simulation results the same method as for the physical test evaluation was used. Therefore, the moment arm and the twisting arm length for the model needed to be found. The lengths in the model are slightly different than in the physical test, because the hubs were not modelled. The y-component of the distance between the two nodes that define the moment arm length was measured within Abaqus to be $d_{moment} = 43.0$ in and the two nodes that define the twisting arm length was measured to be $d_{twist} = 43.65$ in.

The nodal z-displacement of the chassis can be plotted to find the deflection at the front left upright, see Figure 37.

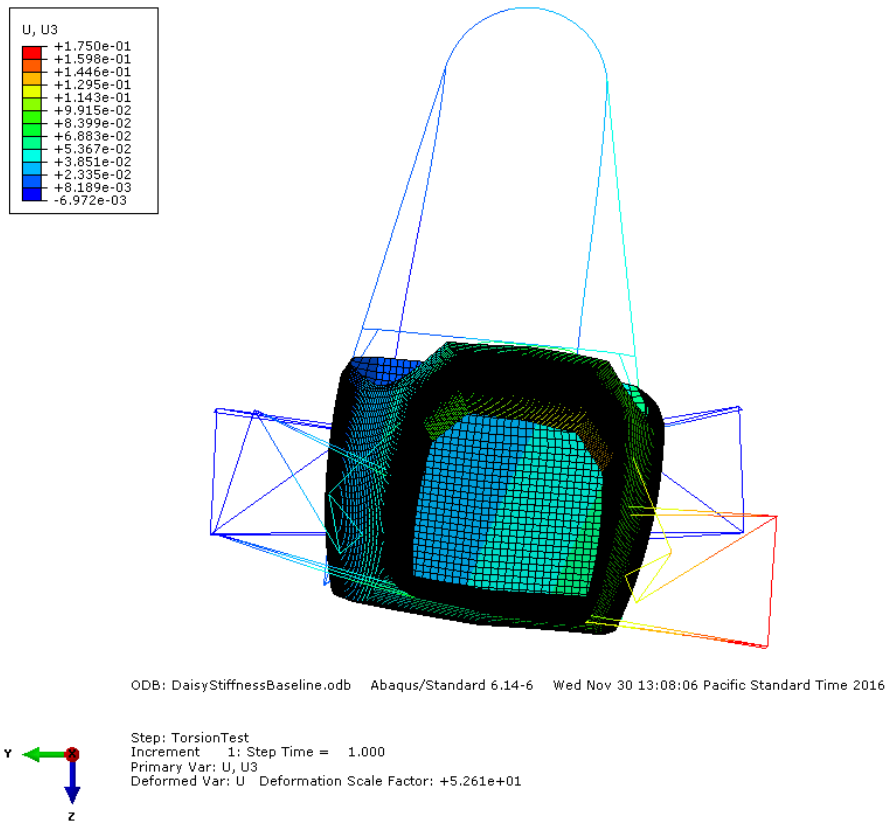

Figure 37: Contour plot of the z-deflection

The deflection result was $\delta_{upright} = 0.175\ in$. The bearing deflection of $\delta_{bearing} = 0.0245\ in$ measured during the physical test that is not included in the model must be added to get a total deflection of $\delta_{total} = 0.1995\ in$. Along with the twisting and moment arm length the torsional stiffness can be calculated to $k_{t,model} = 1381.9\ ft\text{-}lb/deg$.

4.2.7 Comparison and Discussion

The results from the simulation are compared to the physical test for validation. An overview of the torsional stiffness results and the percentage error can be seen in Table 14.

Table 14: Comparison between model and physical test

	Load [lb]	Deflection [in]	Torsional Stiffness [ft-lb/deg]	Percentage Error
Test	100.987	0.232	1308.3	-
Model	100.987	0.1995	1381.9	5.6

It can be seen that the torsional stiffness predicted by the simulation is 5.6 percent higher than the results from the physical test. The difference is mainly due to assumptions made during the modeling process. All the mounts in the model and the test fixture were assumed to be rigid. This is certainly not the case and leads to an over prediction in stiffness. Additionally, it was seen in section 3.3 that the assumptions made by modeling the sandwich structure of the monocoque with effective material properties and as a single surface model made from shell elements lead to stiffer results than the physical test. Due to the setup of the physical test a neutral axis was not clearly defined, so that the distance from the rear fixture to the neutral axis can't be properly represented in the model without modeling the hubs. The lack of hubs in the model leads to a shorter distance between the rear constraints and therefore a stiffer response. Additionally, the elements utilized within the model have a stiffer response than the real material.

4.2.8 Stiffness Distribution

The validated model can be used to find the stiffness distribution along the individual components of the chassis. The chassis can be represented as a series of springs with different stiffness that contribute to the overall stiffness of the system. Breaking down the system into its individual components is necessary to understand its behavior. By changing the individual components of the chassis from deformable to rigid and eliminating their stiffness contribution to the system, the influence of the major components to the overall torsional stiffness can be found.

Additionally, the influence to torsional stiffness of the engine as a stressed member can be found by removing the engine from the chassis and calculating the torsional stiffness without it. This is possible because the engine can be modelled as a spring parallel to the spaceframe. Next, the model can be run with a rigid engine to see how much the overall stiffness increases.

An overview of the results for the torsional stiffness simulation for individually changing the stiffness of the major components to rigid, is given in Table 15.

Table 15: Torsional stiffness of the chassis with rigid components

	Deflection [in]	Torsional Stiffness [ft-lb/deg]	Percentage Change
Baseline	0.1995	1381.9	-
Rigid Suspension	0.1345	2049.7	+ 48.3
Rigid Monocoque	0.129	2137.1	+ 54.7
Rigid Spaceframe	0.0995	2769.9	+ 100.4
Rigid Engine	0.1719	1403.7	+ 1.6
No Engine	0.1995	1251.4	- 9.4

It can be seen that the spaceframe is the softest spring in the system, hence resulting in the largest increase in overall torsional stiffness by a factor of two. If an increase in torsional stiffness is desired, changing the stiffness of the spaceframe has the largest potential.

Both the suspension and the monocoque have an equal effect on the overall torsional stiffness, increasing it by about 50 percent. The torsional stiffness calculated by the model with the rigid suspension equates to the torsional stiffness of the frame, namely k_{frame} = *2049.7 ft-lb/deg*. Knowing the frame stiffness and the overall torsional stiffness, the stiffness of the suspension can be backed out by using the equation for springs in series,

$$\frac{1}{k_{chassis}} = \frac{1}{k_{suspension}} + \frac{1}{k_{frame}}. \tag{4.19}$$

and solving for the suspension stiffness,

$$k_{suspension} = \frac{1}{\frac{1}{k_{chassis}} - \frac{1}{k_{frame}}} = \frac{1}{\frac{1}{1381.9} - \frac{1}{2049.7}} = 4241.5\ \frac{ft-lb}{deg}. \tag{4.20}$$

to get the suspension stiffness of $k_{suspension}$ = *4241.5 ft-lb/deg.*

Comparing the torsional stiffness results without an engine to the results of the model with the rigid engine, two observations can be made. First, the stiffness of the engine is already much higher compared to the other components in the chain, hence the increase in torsional stiffness by 1.5 percent by assuming it being rigid is significantly small. This leads to the assumption that not too much modeling effort should be spent on the engine compared to the other components. Secondly, by the way the engine is mounted to the spaceframe, the overall increase in torsional stiffness by less than 10 percent is small.

5. CHASSIS NATURAL FREQUENCY MODEL

The natural frequency response of a system is driven by its stiffness and mass, or in case of a torsional mode, its polar moment of inertia. The stiffness model of the chassis can therefore be used as the starting point for the natural frequency model.

5.1 Preliminary Considerations

Before starting the modeling process, a couple of considerations about the system should be discussed. The natural frequency response of a system is a combination of the natural frequency responses of each component. As mentioned in section 1.1.2 for the natural frequency response of a system, the rule of octave applies. That means, if components of a system have natural frequencies that are an octave or more apart, they don't influence each other in a significant way and can therefore be analyzed individually.

The chassis can be split it into two major components, the frame and the suspension. The frame is the structure that connects the four parts of the suspension, mainly the monocoque and the spaceframe. Its natural frequency is mainly driven by the stiffness of the structure and its mass. The suspension stiffness, however, is driven by the spring rates and wheel rates. Since those are by the nature of the system the weakest springs. Milliken provides a way of calculating the ride frequency [8], namely the first natural frequency of the suspension considering installed spring stiffness, tire stiffness, motion ratio, unsprung and sprung mass of the vehicle. For the 2016 car, a ride frequency of $f_{suspension} = 2.88\ Hz$ in the front and rear was calculated, which is below the values found in literature for FSAE vehicle frames. Therefore, it can be assumed that natural frequency response of suspension and frame don't interfere with each other and can be modelled as separate systems, respectively. The main advantage, besides simplifying the

model, is that boundary conditions for the frame are known, since they are given by the suspension mounting.

Another aspect to look at are the frequencies excited by components within the vehicle. Two main sources are the engine, which operates at a certain range of speeds which is causing it to vibrate, and the wheels which are an unbalanced rotational mass. The engine operates at speeds from *3000 rpm to 10500 rpm* which equates to a frequency range of *50 Hz to 175 Hz*. The frequency of the wheels is dependent on the velocity of the car. The top speed that the 2016 car will reach is assumed to be about *65 mph* which equates to a frequency of *18 Hz*. Those are the critical frequencies of the system that should be avoided in order to not create resonance.

5.2 Mass Properties and Scaling

To model the mass of the system, the density properties of the used materials must be added to the material definition within Abaqus. Afterwards, the mass of each component can be probed in Abaqus and compared to the physical mass properties taken from the 2016 car. An overview of the material density is displayed in Table 16. The data was taken from datasheets [31], [39], [40] and MatWeb [41].

After probing the calculated mass in Abaqus and comparing it to the measured mass properties of the physical parts the discrepancy was calculated and the density of the material scaled so that the modelled mass matches the physical mass. The difference comes from added tabs and welds on the spaceframe that were not included in the model. The difference for the monocoque comes from ply overlap, film adhesive, core splice, inserts, the missing bulkhead and copper wires that weren't modelled. The shell thickness of the engine was chosen, so that the calculated mass properties would match the physical mass properties. The scaled mass properties are also shown in Table 16.

Table 16: Material density and scaled density

Material	Physical Density [lb_m/in^3]	Scaled Density [lb_m/in^3]
AS4	0.0647	0.0888
M46J	0.0660	0.1266
5052 Aluminum Core	0.0018	0.0023
6061 Aluminum	0.0984	0.0984
4130 Steel	0.2907	0.3315

Additionally, the frame houses most of the components of the car, that are increasing the mass of the system significantly. Instead of modeling the proper geometry of all those components, it is possible to model them as a point mass within Abaqus and assign mass and inertia properties to them. The location for the center of gravity (CG) for each component can roughly be taken from CAD. They can then be moved around in order to match the front-rear weight distribution and the CG height of the car.

Issues were encountered mainly with parts that are difficult to model as point masses, such as the wiring harness, seat belts, cooling lines and fuel lines. Other components, like break lines, control arms, push/push rods, rockers, steer links and half shafts are only partly considered sprung mass, because they are mounted to both the sprung and unsprung mass. Additionally, not all components were modelled in great detail like bolts, nuts mounts, connectors and fittings, but their mass was partly added to the mass of larger components. All this considered, the percentage difference between the actual mass measured on the car to the mass that was modelled is 6.7 percent.

5.3 Boundary Conditions and Constraints

As mentioned earlier, the boundary conditions for the frame are known due to the established connection with the suspension. The definition of the connector elements from section 4.2.3 were replaced with identical boundary conditions. An overview is given in Figure 38.

The tie constraints between the spaceframe and the monocoque and for the engine mounts were transitioned from the torsional stiffness model. Kinematic coupling was chosen to connect the added point masses with the frame. Issues were found to couple all the components in an accurate way, especially components that don't have a separate mount or tab that could be located within the model. Another issue was found in overdefined coupling constraints, for nodes on the frame that were coupled with more than one component. Intense partitioning in those areas was done to solve those errors.

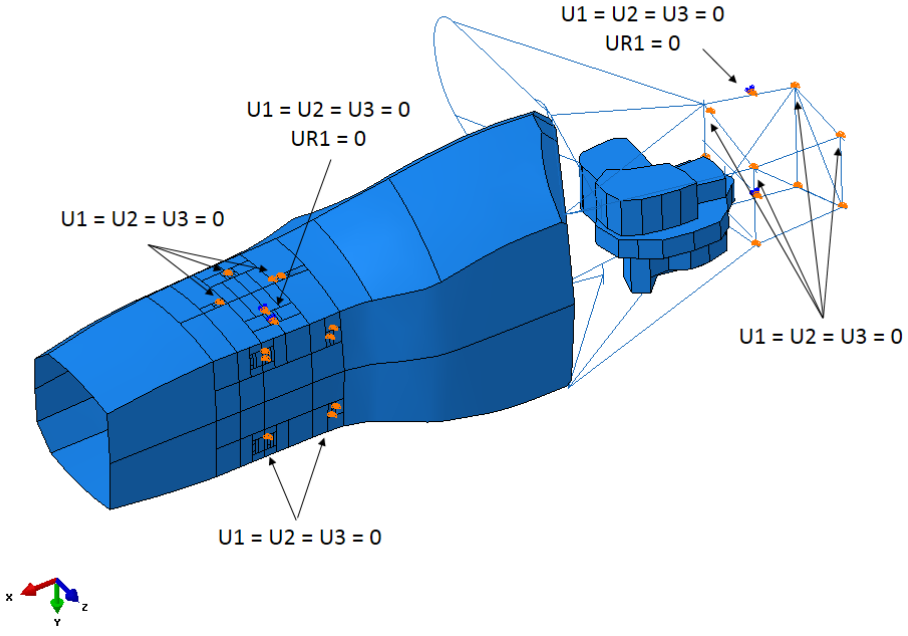

Figure 38: Overview of the boundary conditions

5.4 Results and Discussion

A modal analysis type with a lanczos solver was used to simulate the model. The first run was performed without adding additional components to the frame and without the boundary conditions, so that the results can be compared to the analytical solution. The first twelve modes were extracted, with the first six being rigid body motions, which were ignored. The results are summarized in Table 17.

Table 17: Natural frequency results from the first run

	Frequency [Hz]	Mode Shape
1. Mode	65	1st Bending about y
2. Mode	66	1st Torsion
3. Mode	76	2nd Torsion
4. Mode	111	1st Bending about z
5. Mode	118	3rd Torsion
6. Mode	127	Axial in x

For a comparison, the polar moment of inertia calculated by Abaqus and the frame stiffness calculated in section 4.2.8 were used to calculate the natural frequency for the 1st torsion mode, using

$$f_{1st\ torsion} = \sqrt{\frac{k_{frame}}{I_{p,frame}}} = \sqrt{\frac{1409270\ \frac{in - lb_f}{rad}}{241.5\ lb_f s^2 in}} = 76\ Hz, \tag{5.21}$$

giving a frequency of $f_{1st,\ torsion} = 76\ Hz$ compared to the result from the simulation of

$f_{1st,\ torsion} = 66\ Hz$ leads to a percentage error of *13.2* percent with an absolute error of *10 Hz*.

For the second run the boundary conditions, as described in section 5.3, were added and the first six modes extracted. The results are summarized in Table 18.

Table 18: Natural frequency results from the second run

	Frequency [Hz]	Mode Shape
1. Mode	52	Main Hoop Torsion
2. Mode	89	1st Torsion
3. Mode	91	1st Bending about y
4. Mode	121	2nd Torsion
5. Mode	135	Axial in x
6. Mode	149	2nd Bending about y

As can be seen, adding the boundary conditions stiffens up the structure and increases the frequencies, with the exception of the 1st mode which is the torsion of only the main roll hoop that showed up after adding the boundary conditions.

The third run was performed with the added masses and inertias, but under free vibration without the boundary conditions. The first six modes were extracted and summarized in Table 19.

Table 19: Natural frequency results from the third run

	Frequency [Hz]	Mode Shape
1. Mode	71	1st Bending about y
2. Mode	90	1st Torsion
3. Mode	106	2nd Torsion
4. Mode	114	1st Bending about z
5. Mode	128	3rd Torsion
6. Mode	140	2nd Bending about y

It can be seen, that the frequencies increase from the first run. That result is opposite of the suspected outcome. By adding mass, the polar moment of inertia increases while the torsional stiffness stays the same, which should decrease the frequencies.

As a control value, the 1st mode of torsion can be calculated using the closed form solution and the polar moment of inertia calculated by Abaqus, using

$$f_{1st\ torsion} = \sqrt{\frac{k_{frame}}{I_{p,frame}}} = \sqrt{\frac{1409270\ \frac{in - lb_f}{rad}}{563.4\ lb_f s^2 in}} = 50\ Hz, \tag{5.22}$$

resulting in a frequency of $f_{1st,\ torsion} = 50\ Hz$ which is significantly lower than the result from the simulation and also lower than the calculated value for the frame mass alone.

The fourth run was performed with the added masses and inertias, including the boundary conditions. The first six mode results can be seen in Table 20.

Table 20: Natural frequency results from the fourth run

	Frequency [Hz]	Mode Shape
1. Mode	89	1st Torsion
2. Mode	108	1st Bending about y
3. Mode	117	Axial in x
4. Mode	133	2nd Torsion
5. Mode	164	2nd Bending about y
6. Mode	168	1st Bending about z

Compared to the results from the third run, the frequencies increase due to the stiffening effects of the boundary conditions. However, the frequencies with the added masses was higher than without, which again is not plausible.

In order to determine how Abaqus deals with point masses and added inertia terms, a quick study has been performed, in which the engine was replaced with a point mass of equivalent mass and inertia terms as the modelled engine. The results of the first six modes are displayed in the diagram in Figure 39.

It can be seen that by replacing the engine with a point mass not including inertia terms, the frequencies increase up to 20 percent for the 2nd and 4th mode. Adding in the inertia terms, the results are much closer to the baseline with the engine geometry modelled. However, the frequency of the 2nd mode shows a difference of 37 percent than the base-line value. The trend that can be seen for adding inertia terms is a decrease in frequency across all modes. Given that the inertia terms of all the added components were taken from CAD and not all components were modelled with great detail, the deviation of the results becomes understandable. A more detailed analysis of the inertia is necessary in order to achieve decent results.

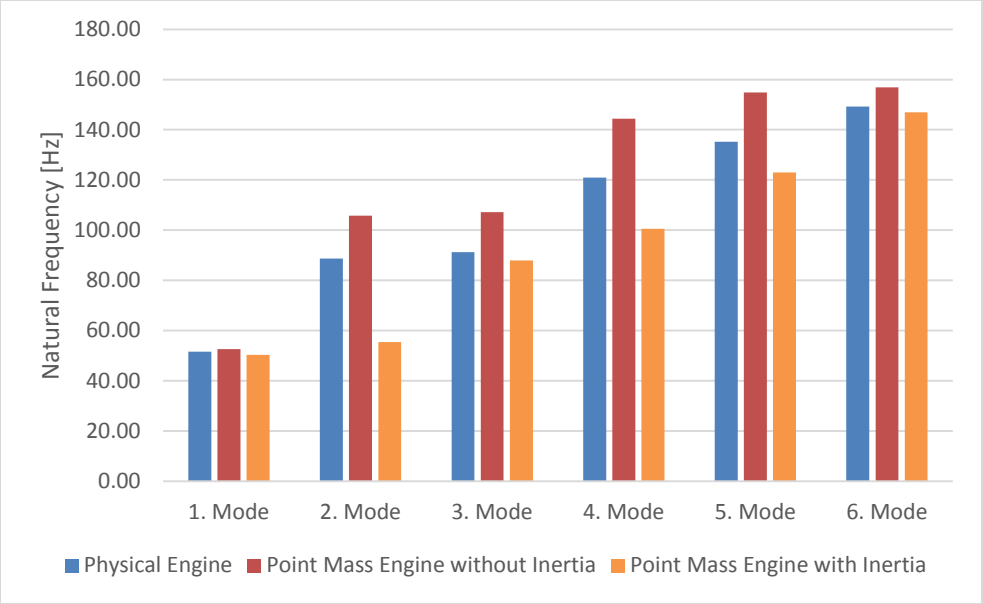

Figure 39: Frequency results for the engine point mass study

5.5 Modal Analysis Conclusion

Looking back to the initial goal of determining the cause for the cracking engine mounts, the calculated natural frequencies must be compared to the systems critical frequencies. Although the quantitative results of the frequencies are questionable, a few conclusions can be drawn from the shape of the modes and the range of frequencies that have been found in the course of the study.

The first thing to note is that the imbalanced mass of the wheels doesn't excite the frame, because even at an assumed maximum velocity of *65 mph* the frequency of *18 Hz* is still much lower than the first mode of the frame. The frequency range of 50 Hz – 175 Hz that the engine excites however, is much likely within in the range of the natural frequencies of the frame, if the 1st torsional mode is in the range around 60 Hz. Especially the deformation shape of the 1st and 2nd torsional mode, displayed in Figure 40 and Figure 41, show that the twist of the engine is opposite of the twist of the space-

frame around it. The high strain that is created in the engine mounts due to the opposite translation can lead to cracks, especially at low frequencies that have high amplitudes that result in large deformations that cause high stresses.

Apart from the damage in the engine mounts, that have been solved in 2016 by adding an extra mount to the engine distributing the reaction forces into three mounts except two decreasing the stresses in each mount, the resonance of the frame can cause issues passing the noise test at competition. Due to the FSAE rules, the noise output is taken at idle, which for the recent engine is around 3500 rpm, and 7000 rpm [1]. Those speeds correspond to ~60 Hz and 125 Hz that lie within the resonance range of the frame.

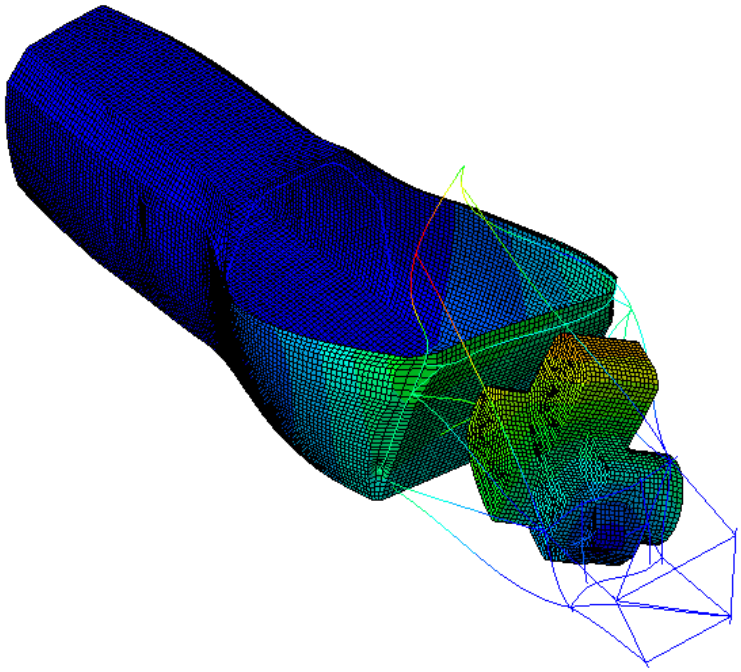

Figure 40: Shape of the 1st torsional mode

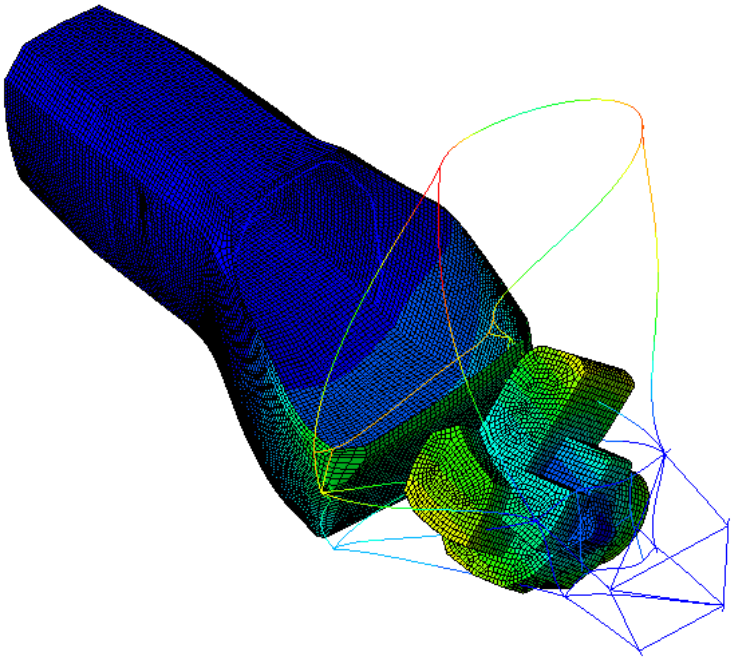

Figure 41: Shape of the 2nd torsional mode

6. CONCLUSION

The goal of the thesis was to exploit a way to accurately predict the torsional stiffness of a carbon fiber reinforced polymer hybrid chassis using finite element analysis and modeling the natural frequency response to find the potential cause for the damage in the engine mounts.

It has been shown that accurate material properties for carbon fiber reinforced polymer materials must be collected through testing to predict accurate results with the simulation. It has been found that due to different layup and curing methods, resulting in voids and elevated resin content, the stiffness response can vary up to 30 percent compared to published values. The constitutive response of hexagonal cell core can be taken from datasheets since mainly the out-of-plane properties matter to model the stiffness characteristics of a sandwich structure. Values for the in-plane properties are very low but must be adjusted in order to satisfy the restrictions of the stiffness tensor for orthotropic materials.

By modeling a simple three-point-bend test of a sandwich panel the tested properties can be tuned to match test results. High sensitivity to the deflection of the panel for the ply thickness was found. Great effort should be made measuring panel thickness to find the proper thickness for the plies and the core. Working with effective material response instead of modeling the micro-structure of the material was proven to work. The stiffness of the sandwich structure is driven by Young's modulus in the fiber direction of the face sheet, the in-plane shear modulus of the face sheet and the out-of-plane shear moduli of the core. The use of conventional shell elements with shear deformation to model the sandwich structure has been found to work, if solid elements lead to unacceptably high modeling and computational effort.

The torsional stiffness prediction of the chassis could be validated with a physical test with a percentage error of 5.6 percent. The overestimation in stiffness is due to modeling assumptions and assumed rigid mounts. The deflection of the bearings in the suspension had a large effect on the results. Closer examination of the compliance in each bearing is necessary to achieve closer and more reliable results. A large emphasis was placed on the accurate representation of connections in the suspension and the connections to the frame. A method to check if the connections work accordingly is to check section forces and moments in suspension members to make sure they are not subject to bending moments. Another important aspect to consider is the correct representation of the area of influence for the mounts. Partitioning can be used to create proper size areas on the surface to which the mount is connected to.

Using the torsional stiffness model and adding density properties to simulate the natural frequency response of the frame lead to plausible results when comparing them to published values from other FSAE vehicles with similar stiffness to weight ratio frames and results from the analytical solution. The first mode for the frame without additional components can therefore be found around 52 Hz. The results for the frame model can be used as a reference value for the development of future chassis structures in order to determine how the natural frequency range changed. Adding masses for the components that are housed in the frame however, lead to an increase in natural frequency which is opposite of the assumed outcome. The analytical solution suggests a frequency of 50 Hz for the first torsional mode for the frame with added components which is plausible value. It has been found that the inertia terms of the point masses have a big effect on the frequency results.

A test on the full car that has been done last year found frequency spikes around 40 Hz and 60 Hz. Despite the uncertainty of the quantitative result of the natural frequencies, by studying the deformation modes for the 1st and 2nd torsion mode, high deformations between the spaceframe and the engine can be seen, that can lead to damage in the mounts. Considering the physical test and the result from the closed form solution suggest that it is highly likely that the operating range of the engine lies within the resonance range of the frame, causing the above mentioned deformation modes. Another concern arises from the engine noise that can be amplified by creating resonance with the frame, especially for the two tested speed ranges of 3500 rpm and 7000 rpm for the noise test specified by the FSAE rules, that lie well within the resonance range of the frame.

7. FUTURE WORK

More three-point-bend tests should be performed in order to be able to introduce statistical analysis to find reasonable ply and core thickness values and find a correlation between the thickness of the plies and the stiffness of the panel for different layups. The manufacturing method of the face sheets could have a significant influence on the specific stiffness of the panel.

To achieve more accurate values through the torsional stiffness simulation, the stiffness of connections and mounts should be looked at closer. Efforts to model bolted composites joints were made in this thesis but didn't lead to reliable results. Testing different designs is better way to find the stiffness of the bolted connection. The mounts can be analyzed using CAE methods. The connector elements offer the option to define the local stiffness of the mounts, which is a more efficient way to include their stiffness than including the mounts in the global model. Additionally, the fixture should be included in the model to include its compliance.

A way to perform proper measurements of the deflection in each individual bearing need to be found. Once the compliance in a single bearing is known, it is possible to sum them up to find the accurate overall bearing deflection.

The natural frequency of the chassis is best determined by a test that can then be used to tune the model. This can be done by adjusting inertia terms and redefining the couple connections of the components to the frame. The resultant modes can be used to find areas where stiffeners increase the frequency accordingly. The results for the frame frequency alone can be used as a comparison for future frames to compare the specific stiffness development.

BIBLIOGRAPHY

[1] S. International, "Formula SAE Rules 2016," 07 09 2016. [Online]. [Accessed 14 10 2016].

[2] William B. Riley, Albert R. George, "Design, Analysis and Testing of a Formula SAE Car Chassis," *SAE Technical Paper Series,* 2002.

[3] Pang Shu-Yi, Guan Xin, Zhan Jun, "Research of Chassis Torsional Stiffness on Vehicle Handling Perfomance," *WASE International Conference on Information Engineering,* pp. 253-256, 2010.

[4] Andrew Deakin, David Crolla, Juan Pablo Ramirez, Ray Hanley, "The Effect of Chassis Stiffness on Race Car Handling Balance," *SAE Technical Papers,* 2000.

[5] G. Mirone, "Multi-Body Elastic Simulation of a Go-Kart: Correlation between Frame Stiffness and Dynamic Performance," *International Journal of Automotive Technology,* vol. 11, no. 4, pp. 461-469, 2010.

[6] Oskar Danielsson, Alejandro Gonzalez Cocana, "Influence of Body Stiffness on Vehicle Dynamics Characteristics in Passenger Cars," Chalmers University of Technology, Goeteborg, Sweden, 2015.

[7] H. Heisler, Advanced Vehicle Technology, Woburn: Butterworth-Heinemann, 2002.

[8] William F. Milliken, Douglas L. Milliken, Race Car Vehicle Dynamics, Warrendale:

Society of Automotive Engineers, 1995.

[9] Carl Andersson Eurenius, Niklas Danielsson, Aneesh Khokar, Erik Krane, Martin Olofsson, Jacob Wass, "Analysis of Composite Chassis," Chalmers University of Technology, Goeteborg, Sweden, 2013.

[10] Andrew Cunningham, Andrew Ferrell, Matthew Lee, Tony Loogman, "Formula Monocoque Development," California Polytechnic State University, San Luis Obispo, 2015.

[11] Evan Jenkins, Dave Baker, Matt Grusenmeyer, Shane Marcks, Adam Baldan, "FSAE Chassis: Phase iV Report," University of Delaware, Delaware, 2010.

[12] Javier Gutierrez, Angel Nunez, Diego Qintero, "Development of a Formula SAE Body," Florida International University, Florida, 2013.

[13] B. Lii, "Design and Manufacturing of a Composite Monocoque Chassis," University of Queensland, Brisbane, Australia, 2009.

[14] R. P. Singh, "Structural Performance Analysis of Formula SAE Car," *Jurnal Mekanikal,* no. 31, pp. 46-61, 2010.

[15] Matthew Hagan, John Rappolt, John Waldrop, "Formula SAE Hybrid Carbon Fiber Monocoque/Steel Tube Frame Chassis," California Polytechnic State University, San Luis Obispo, 2014.

[16] S. S. Rao, Mechanical Vibrations, Prentice Hall, 2011.

[17] R. Abrams, "Formula SAE Race Car Analysis: Simulation and Testing of the Engine as a Structural Member," The University of Western Ontario, Ontario,

Canada, 2008.

[18] Mohammad Al Bukhari Marzuki, Mohammad Hadi Abd Halim, Abdul Razak Naina Mohamed, "Determination of Natural Frequencies through Modal and Harmonic Analysis of Space Frame Race Car Chassis based on ANSYS," *American Journal of Engineering and Applied Sciences,* 2015.

[19] Mehdi Mahmoodi-k, Iraq Davoodabadi, Vinko Visnjic, Amir Afkar, "Stress and Dynamic Analysis of Optimized Trailer Chassis," *Tehnički vjesnik,* vol. 3, no. 21, pp. 599-608, 2014.

[20] eFunda, Inc., "Lamina Principal Directions," eFunda, Inc., [Online]. Available: http://www.efunda.com/formulae/solid_mechanics/composites/images/Lamina_PrincipalDir.gif. [Accessed 20 10 2016].

[21] G. Thomas Mase, Ronald E. Smelser, George E. Mase, Continuum Mechanics for Engineers, Taylor and Francis Group, 2010.

[22] Bhagwan D. Agarwal, Lawrence J, Broutman, Analysis and Perfomance of Fiber Composites, Wiley, 2006.

[23] Vlado A. Lubarda, Michelle C. Chen, "On the Elastic Moduli and Compliances of Transversly Isotropic and Orthotropic Materials," *Journal of Mechanics of Materials and Structures,* vol. 3, no. 1, pp. 153-171, 2008.

[24] A. International, "Standard Test Method for Tensile Properties of Polymer Matrix Composite Materials," D3039, West Comshohocken, PA, 2014.

[25] V. M. Measurements, "General Purpose Strain Gages - Tee Rosette," VishayPG, [Online]. Available: http://www.vishaypg.com/docs/11300/250ut.pdf. [Accessed 28

10 2016].

[26] VishayPG, "Strain Gage Installations with M-Bond 200 Adhesive," Instruction Bulletin B-127-14.

[27] A. International, "Standard Test Method for In-Plane Shear Response of Polymer Matrix Composite Materials by Tensile Test of a ±45° Laminate," D3518, West Conshohocken, PA, 2013.

[28] Department of Defense, "Volume 1: Polymer Matrix Composites," in *Composite Materials Handbook*, Department of Defense, 1997.

[29] F. E. Penado, "Effective Elastic Properties of Honeycomb Core with Fiber-Reinforced Composite Cells," *Open Journal of Composite Materials,* vol. 3, pp. 89-96, 2013.

[30] Ilke Aydincak, Altan Kayran, "An Approach for the Evaluation of Effective Elastic Properties of Honeycomb Cores by Finite Element Analysis of Sandwich Panels," *Journal of Sandwich Structures and Materials,* vol. 11, pp. 385-408, 2009.

[31] Hexcel, "HexWeb Honeycomb Sandwich Design Technology," Hexcel Composites, Duxford, 2000.

[32] A. International, "Standard Test Method for Flatwise Compressive Properties of Sandwich Cores," ASTM International, 1994.

[33] C. W. Schwingshackl, G.S. Aglietti, P.R. Cunningham, "Determination of Honeycomb Material Properties: Existing Theories and an Alternative Dynamic Approach," *Journal of Aerospace Engineering,* vol. 19, no. 3, pp. 177-183, 2006.

[34] Imran Ali, Yu Jing Jun, "Mathematical Models for in-plane Moduli of Honeycomb Structures - A review," *Research Journal of Applied Sciences, Engineering and Technology,* vol. 7, no. 3, pp. 581-592, 2014.

[35] G. A. Hoffman, "Poisson's Ratio for Honeycomb Sandwich Cores," *Journal of the Aerospace Sciences,* vol. 25, no. 8, pp. 534-535, 1958.

[36] Stephen King, Tony Richards, *Solving Contact Problems with Abaqus,* Coventry: Dassault Systemes, 2013.

[37] D. Systèmes, *Abaqus 6.13 User's Manual,* Providence: Dassault Systèmes Simulia Corp., 2013.

[38] N. Powell, "Cal Poly Racing 2016 Chassis Overview "Daisy"," 2016.

[39] Torayca, "M46J Data Sheet," [Online]. Available: http://www.toraycfa.com/pdfs/M46JDataSheet.pdf. [Accessed 01 12 2016].

[40] Hexcel, "HexTow AS4 Product Datasheet," 2015. [Online]. Available: http://www.hexcel.com/resources/datasheets/carbon-fiber-data-sheets/as4.pdf. [Accessed 01 12 2016].

[41] ASM Aerospace Specification Metals, Inc., "ASM MatWeb," [Online]. Available: http://www.aerospacemetals.com/index.html. [Accessed 12 10 2016].

[42] P. A. Renuke, "Dynamic Analysis Of A Car Chassis," *International Journal of Engineering Research and Applications,* vol. 2, no. 6, pp. 955-959, 2012.

[43] E. C. Anderson, "Design and Optimization of Carbon-Fiber Chassis Panels," Virginia Polytechnic Institute and State University, Blacksburg, 2014.

[44] David C. Weggel, David M . Boyajin, Shen-En Chen, "Modelling structures as systems of springs," *World Transactions on Engineering and Technology Education,* vol. 6, no. 1, pp. 169-172, 2007.

[45] Jospeh Penzien, Theodor Didriksson, "Effective Shear Modulus of Honeycomb Cellular Structure," *AIAA Journal,* vol. 2, no. 3, pp. 531-535, 1964.

[46] R. Rajappan, M. Vivekanandhan, "Static and Modal Analysis of Chassis by using FEA," *International Journal of Engineering and Science,* vol. 2, no. 2, pp. 63-73, 2013.

[47] Wang Wenlin, Cheng Siyuan, Luo Mingjun, "Experimental Modal Test for Structure Refinement of an Automotive Chassis," *International Conference on Measuring Technology and Mechatronics Automation,* pp. 174-177, 2010.

APPENDIX A

Material Properties Calculations for Tensile Composites Testing

Equations taken from ASTM D3039 Created: 04/26/2016 Manuel Herrmann Last Edited: 10/28/2016

```
clc, clear, close all
```

Import Tension Testing Data from Excel for Tensile Specimen (0 or 90)

reading the raw datafile

```
filename = 'run12.txt';
% filename = input('Name of the data file: ', 's');
fileID = fopen(filename);
D = textscan(fileID,'%f %f %f %f');
fclose(fileID);

% saving the raw data
Load_raw = D{1}; % raw load curve data
Extensometer_raw = D{2}; % raw lateral extensometer data
Axial_raw = D{3}; % raw lateral strain gauge data
Transverse_raw = D{4}; % raw transverse strain gauge data

% Userinput - Cross-Section Area of the specimen
% A = input('Cross-Section Area of the Specimen in squared inches: ');
t = 0.046; % measured thickness of the specimen in inch
W = 0.529; % measured width of the specimen in inch
A = W*t;
```

Finding Start and End of Test

```
[maxload, imax] = max(Load_raw);
Maxload = Load_raw(1:imax);
[sortedX,sortingIndices] = sort(diff(Maxload),'descend');
imin = sortingIndices(7);
Minload = Maxload(imin:end);
```

Creating Plots for the Development

plotting sorted slopes figure(1) plot(sortedX(1:200),'.-') hold on plot(7,sortedX(),'o')

```
% plotting cutted load curve
% figure(2)
% % plot(Load)
% hold on
% plot(Minload,'k')
% % stack fitted curve
% X = 1:length(Minload);
% [p] = polyfit(X,Minload',1);
% xvalues = 0:length(Minload);
% yvalues = polyval(p,xvalues);
% hold on
% plot(xvalues,yvalues,'--')
```

data correction

```
Offset = 0 + Axial_raw(1); % calculating the offset
Axial = Axial_raw(imin:imax) - Offset; % Correcting the Offset & cutting dataset
Offset = 0 + Transverse_raw(1); % calculating the offset
Transverse = Transverse_raw(imin:imax) - Offset; % Correcting the Offset & cutting dataset
Load = Load_raw(imin:imax);
% Offset = 0 + Extensometer_raw(1);
% Extensometer = Extensometer_raw - Offset;
```

Plotting Force and Strain Curves

figure(3) plot(Load) figure(4) plot(Axial) figure(5) plot(Transverse)

Plot Stress vs Strain Curve

```
figure(6)
Stress = Load/A; % in psi
plot(Axial,Stress)
hold on
pars = fit(Axial,Stress,'poly1');
plot(pars)
axis square
title('Stress vs Strain')
xlabel('Normal Strain \epsilon_1 [microstrain]')
ylabel('Normal Stress \sigma_1 [psi]')
legend('raw data', 'fitted curve', 'location', 'NorthWest')
xpos=2000;
ypos=150000;
txt1 = {[num2str([pars.p1]) 'x '  num2str([pars.p2])]};
text(xpos,ypos,txt1)
hold off
```

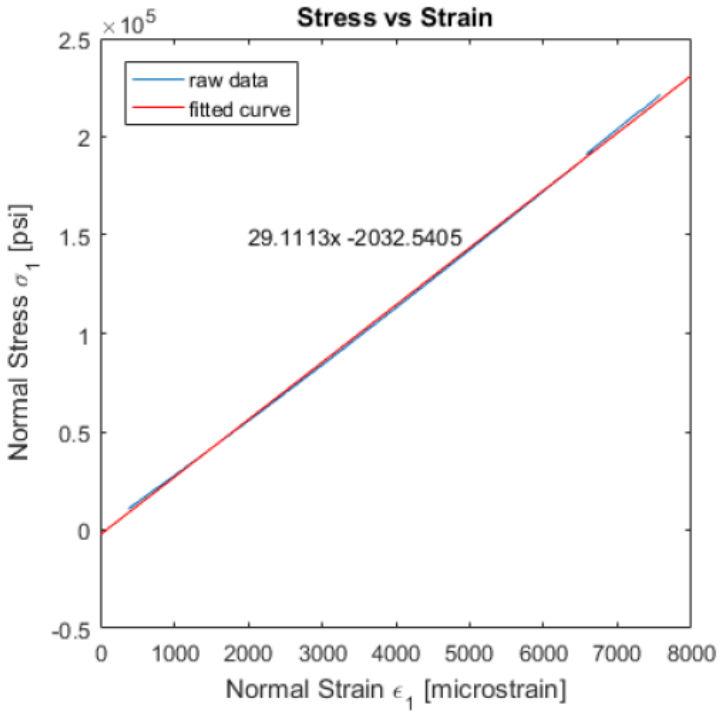

Plot Normal vs Transverse Strain

```
figure(7)
plot(Axial,Transverse)
hold on
pars = fit(Axial,Transverse,'poly1');
plot(pars)
axis square
title('Normal vs Transverse Strain')
xlabel('Normal Strain \epsilon_1 [microstrain]')
ylabel('Transverse Strain \epsilon_2 [microstrain]')
legend('raw data', 'fitted curve', 'location', 'NorthEast')
xpos=4000;
ypos=-800;
txt1 = {[num2str([pars.p1]) 'x '  num2str([pars.p2])]};
text(xpos,ypos,txt1)
hold off
```

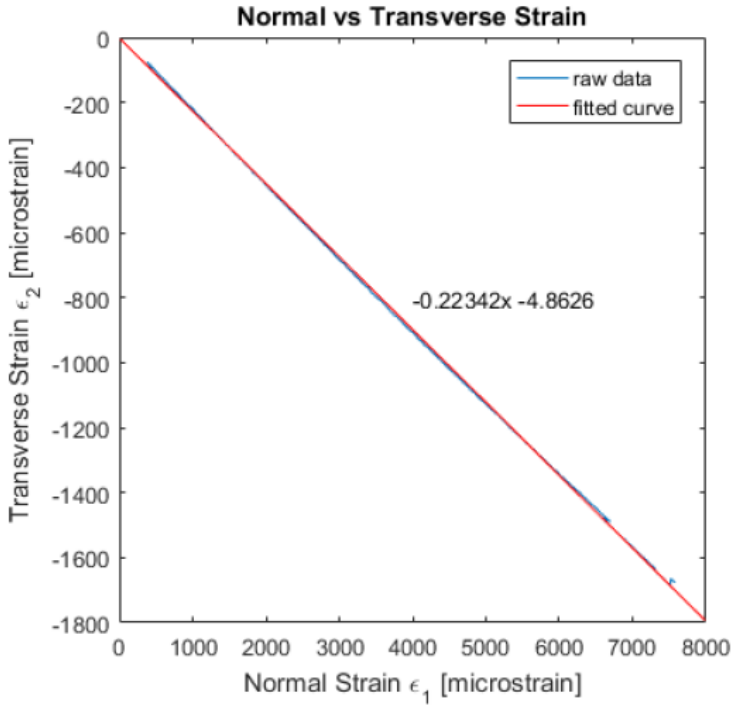

Calculating Material Properties from the Data

calculating the E-Modulus in the lateral direction

```
E1 = (Load(end)/A - Load(1)/A)/(Axial(end)*1e-6 - Axial(1)*1e-6);
display('The Modulus in the lateral direction in psi: ')
fprintf('%7.2f',E1)
fprintf('\n')
% calculating the major Poisson`s ratio
v12 = -(Transverse(end) - Transverse(1))/(Axial(end) - Axial(1));
display('The major Poisson`s ratio: ')
fprintf('%1.4f',v12)
fprintf('\n')
% calculating the ultimate tensile Strength in the lateral direction
F1t = Load(end)/A;
display('The ultimate Strength in the lateral direction in psi: ')
fprintf('%7.2f',F1t)
fprintf('\n')
% calculating the max tensile strain in the lateral direction
e1t = Axial(end);
display('The ultimate tensile strain in micro strains is: ')
fprintf('%7.2f',e1t)
fprintf('\n')
```

```
The Modulus in the lateral direction in psi:
29210815.78
The major Poisson`s ratio:
```

```
0.2213
The ultimate Strength in the lateral direction in psi:
221375.98
The ultimate tensile strain in micro strains is:
7588.26
```

Published with MATLAB® R2016a

APPENDIX B

Material Properties Calculations for In-Plane Shear Composites Testing

Equations taken from ASTM D3518 Created: 04/26/2016 Manuel Herrmann Last Edited: 10/28/2016

```
clc, clear, close all
```

Import Tension Testing Data from Excel for In-Plane Shear Specimen (+-45)

reading the raw datafile

```
filename = 'run115.txt';
% filename = input('Name of the data file: ', 's');
fileID = fopen(filename);
D = textscan(fileID,'%f %f %f %f');
fclose(fileID);

% saving the raw data
Load_raw = D{1}; % raw load curve data
Extensometer_raw = D{2}; % raw lateral extensometer data
Axial_raw = D{3}; % raw lateral strain gauge data
Transverse_raw = D{4}; % raw transverse strain gauge data

% Userinput - Cross-Section Area of the specimen
% A = input('Cross-Section Area of the Specimen in squared inches: ');
t = 0.143; % measured thickness of the specimen in inch
W = 0.87; % measured width of the specimen in inch
A = W*t;
```

Finding Start and End of Test

```
[maxload, imax] = max(Load_raw);
Maxload = Load_raw(1:imax);
[sortedX,sortingIndices] = sort(diff(Maxload),'descend');
imin = sortingIndices(2);
Minload = Maxload(imin:end);
```

Creating Plots for the Development

% plotting sorted slopes figure(1) plot(sortedX(1:200),'-') hold on plot(5,sortedX(),'o')

```
% % plotting cutted load curve
% figure(2)
% % plot(Load)
% hold on
% plot(Minload,'k')
% % stack fitted curve
% X = 1:length(Minload);
% [p] = polyfit(X,Minload',1);
% xvalues = 0:length(Minload);
% yvalues = polyval(p,xvalues);
% hold on
% plot(xvalues,yvalues,'--')
```

data correction

```
Offset = 0 + Axial_raw(1); % calculating the offset
Axial = Axial_raw(imin:imax) - Offset; % Correcting the Offset & cutting dataset
Offset = 0 + Transverse_raw(1); % calculating the offset
Transverse = Transverse_raw(imin:imax) - Offset; % Correcting the Offset & cutting dataset
Load = Load_raw(imin:imax);
% Offset = 0 + Extensometer_raw(1);
% Extensometer = Extensometer_raw - Offset;
```

Plotting the corrected Load and Strain Curves

figure(3) plot(Load) figure(4) plot(Axial) figure(5) plot(Transverse)

Calculating Material Properties from the Data

calculate the shear strain data

```
Shear = Axial-Transverse;
% find the range of strain from 1500 to 2500 micro strains
strainrange = find(Shear-1500 > 0 & Shear-5500 < 0);
% Calculating In-Plane Shear Modulus (linear region)
G12 = (Load(strainrange(end))/(2*A) - Load(strainrange(1))/(2*A)) /...
     ((Shear(strainrange(end))*1e-6 ) - (Shear(strainrange(1))*1e-6));
display('The In-Plane Shear Modulus in psi: ')
fprintf('%7.2f',G12)
fprintf('\n')
% Calculating ultimate In-Plane Shear Strength
F6 = Load(end)/(2*A);
display('The ultimate In-Plane Shear Strength in psi: ')
fprintf('%7.2f',F6)
fprintf('\n')
% Calculating max shear strain
e12 = Shear(end);
display('The ultimate shear strain  in micro strains is: ')
```

```
fprintf('%7.2f',e12)
fprintf('\n')
```

```
The In-Plane Shear Modulus in psi:
488322.31
The ultimate In-Plane Shear Strength in psi:
8776.78
The ultimate shear strain  in micro strains is:
26286.90
```

Calculating Laminate Properties

calculating the laminates E-Modulus in the lateral direction

```
Ex = (Load(strainrange(end))/A - Load(strainrange(1))/A)/...
     (Axial(strainrange(end))*1e-6 - Axial(strainrange(1))*1e-6);
display('The Modulus in the lateral direction of the laminate in psi is: ')
fprintf('%7.2f',Ex)
fprintf('\n')
% calculating the lamintes major Poisson`s ratio
vxy = -(Transverse(strainrange(end)) - Transverse(strainrange(1)))/...
       (Axial(strainrange(end)) - Axial(strainrange(1)));
display('The major Poisson`s ratio of the laminate is: ')
fprintf('%1.2f',vxy)
fprintf('\n')
```

```
The Modulus in the lateral direction of the laminate in psi is:
1809113.66
The major Poisson`s ratio of the laminate is:
0.85
```

Plot Stress vs Strain

```
SStress = Load/(2*A);
figure(6)
plot(Shear,SStress)
hold on
X_range = 1:length(strainrange);
SStress_lin = Load(strainrange)/(2*A);
lin_shear = Shear(strainrange);
pars = fit(lin_shear,SStress_lin,'poly1');
plot(pars,'r')
hold off
axis square
title('Shear Strain vs Shear Stress')
xlabel('Engineering Shear Strain \gamma_1_2 [microstrain]')
ylabel('Shear Stress \tau_1_2 [psi]')
legend('raw data', 'linear region', 'location', 'NorthWest')
xpos=9000;
ypos=10000;
txt1 = {[num2str([pars.p1]) 'x + '  num2str([pars.p2])]};
```

```
text(xpos,ypos,txt1)
```

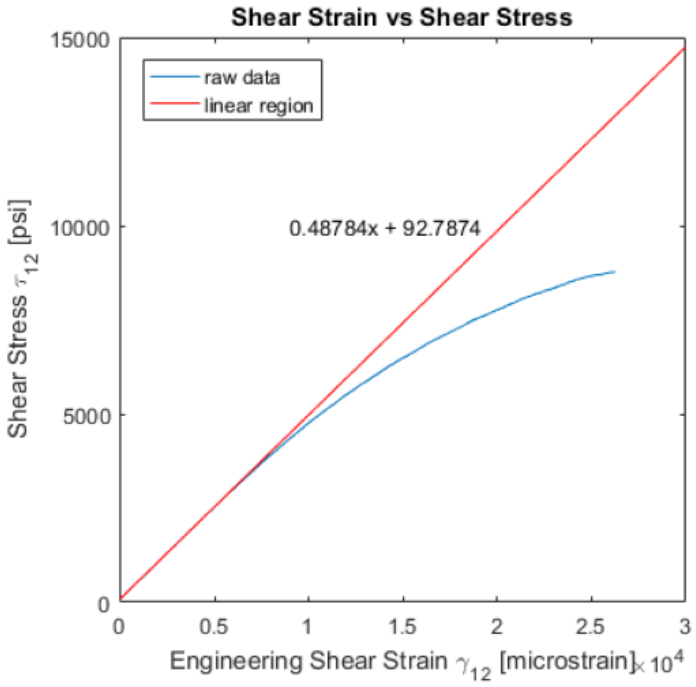

Export to Excel

```
P = [Shear Load/(2*A)]; filename = 'ShearStress-ShearStrainData.xls'; xlswrite(filename, P)
```

Published with MATLAB® R2016a

APPENDIX C

Classical Laminate Theory - three-point-bend test

created: 30/04/2016 Manuel Herrmann last edited: 19/09/2016

```
clear, clc, close all
```

toggle switch

```
toggle = 0;

% toggle = 0: evaluate for a single value only
% toggle = 1: plot core thickness graph
% toggle = 2: plot skin thickness graph
```

Material Database

all units in US customary (lb, in, s) properties needed: E1 E2 G12 v12 a11 a22 rho E1 E2 G12 v12 a11 a22 F1t F2t F12 F1c F2c e1t e2t e12 e1c e2c

```
M = [.057     20e06     1.4e06    .93e06   .3     -.5e-6   15e-6    280e03   8.3e03   10.3e03
  240e03 33e03  .014   .007 .0296  .012  .031; % Carbon Epoxy AS4/3501-6 (unidirectional tape
)
     .066     28.77e06  0.787e06  .48e06   0.226  -.5e-6   15e-6    221e03   0        0
  0      0      .0076  0    .0024  0     0   ; % Carbon Epoxy M46J/TC250 (unidirectional tape
)
     0.00179  89.62     46.80     4.46     1      22045.7  44961.7  130.534  210.305  333.587

  0      0      0      0    0      0     0  ]; % 5052 Aluminum Honeycomb Core
%    rho       E1        E2        G12       v12     G23 (W)   G23 (L)   F23(W)    F23 (L)   F3
  F1c     F2c     e1t     e2t   e12     e1c    e2c
```

Laminate Definition

Define angle, thickness and material of each ply in the laminate [angle thickness matl #]

```
if toggle == 0
    cthick = 0.69;      % core thickness
    pthick = .0058;      % ply thickness
end

if toggle == 1
    cthick = [.65 .66 .67 .68 .69 .7 .71 .72 .73 .74 .75];  % core thickness
    pthick = 0.008;                                          % ply thickness
end

if toggle == 2
    cthick = 0.7;                                                    % core thickness
    pthick = [.004 .0045 .005 .0055 .006 .0065 .007 .0075 .008];     % ply thickness

end

% Sweep through core thickness and density
for k = 1 : length(cthick)
for kk = 1 : length(pthick)
```

```
L = [ 45.0  pthick(kk)      2;
      0.0    pthick(kk)     2;
      -45.0   pthick(kk)     2;
      0.0    cthick(k)       3;
      -45.0   pthick(kk)     2;
      0.0    pthick(kk)     2;
      45.0  pthick(kk)     2];
% material #1: Carbon Epoxy AS4/3501-6 (unidirectional tape)
% material #2: Carbon Epoxy M46J/TC250 (unidirectional tape)
% material #3: 5052 Aluminum Honeycomb Core



% get number of plies
n = size(L,1);
% find the total thickness
thick = sum(L(:,2));
```

Load Input

mechanichal line loads specifically for 3-point-bend test w/ central load & simple support on both ends

```
Force = 972.6;   % applied force in lb
span = 19.685; % Span of the test fixture in inches
```

```
width = 10.8268; % Width of the panel in inches
Mx = Force*span/(4*width);
%         Nx      Ny      Nxy     Mx    My      Mxy
load_m = [0;      0;      0;      Mx;   0;      0];
% thermal loads
delT = 0; % temperature change in Fahrenheit
```

Setting up the ABD Matrix

Initializing Sub-Matrices

```
h = zeros(n+1,1);
A = zeros(3);
B = zeros(3);
D = zeros(3);
N_t = zeros(3,1);
M_t = zeros(3,1);
FIF = zeros(1,3);

% Form R matrix which relates engineering to tensor strain
R = [1  0  0; 0  1  0; 0  0  2];

% locate the bottom of the first ply
h(1) = -thick/2.;
imax = n + 1;

% loop for rest of the ply distances from midsurface
for i = 2 : imax
   h(i) = h(i-1) + L(i-1,2);
end
```

```
    % loop over each ply to integrate the ABD matrices
    for i = 1:n

        % ply material ID
        mi = L(i,3);    % grab material number from the laminate definition
        v21 = M(mi,3)*M(mi,5)/M(mi,2);
        D_s = 1 - M(mi,5)*v21;

        % Q12 matrix
        Q = [M(mi,2)/D_s          v21*M(mi,2)/D_s    0;
             M(mi,5)*M(mi,3)/D_s  M(mi,3)/D_s        0;
             0                    0                  M(mi,4)];

        % ply angle in radians
        theta = L(i,1)*pi/180;

        % form transformation matrices T1 for ply
        T1 = [(cos(theta))^2          (sin(theta))^2           2*sin(theta)*cos(theta);
              (sin(theta))^2          (cos(theta))^2          -2*sin(theta)*cos(theta);
              -sin(theta)*cos(theta)   sin(theta)*cos(theta)  (cos(theta))^2-(sin(theta))^2 ]
;
        % form T2 for thermal
        T2 = R*T1*inv(R);
```

```
        % form Qxy
        Qxy = inv(T1)*Q*R*T1*inv(R);

        % build up the laminate stiffness matrices
        A = A + Qxy*(h(i+1)-h(i));
        B = B + Qxy*(h(i+1)^2 - h(i)^2);
        D = D + Qxy*(h(i+1)^3 - h(i)^3);

        % load alphas into an array
        a = [M(mi,6); M(mi,7); 0.0];

        % Calculate thermal loads
        N_t = N_t + delT*Qxy*inv(T2)*a*(h(i+1) - h(i));
        M_t = M_t + delT*Qxy*inv(T2)*a*(h(i+1)^2 - h(i)^2);

        % calculate mass of the panel
        ply_mass(i) = M(mi,1) * L(i,2) * width * span;
        if toggle == 0
            mass(k) = sum(ply_mass);
        end
        if toggle == 1
            mass(k) = sum(ply_mass);
        end
        if toggle == 2
           mass(kk) = sum(ply_mass);
        end

    end
```

Build Stiffness and Compliance Matrix

change the display format

```
format short e
B = (1/2)*B;
D = (1/3)*D;
M_t = (1/2)*M_t;
% assemble the stiffness Matrix
K = [A, B;
     B, D];
% calculate the compliance matrix
C = inv(K);
```

Calculate the Deflection of the Beam

thickness to middle of facesheets (distance is h in Hexcel design guide)

```
    if toggle == 2
        distance = (thick+cthick)/2;
    end

    if toggle == 1
        distance = (thick+cthick(k))/2;
    end
```

```
    if toggle == 0
        distance = (thick+cthick(k))/2;
    end

% wide and narrow effective stiffness
EIn = width/C(4,4);
EIw = width*K(4,4);

% bend stiffness
kbn = 48*EIn/span^3;
kbw = 48*EIw/span^3;

% shear stiffness
ks = width*distance*M(3,6);

% shear deflection
ds = 0.25*Force*span/ks;

% bending deflection narrow and wide beam
dbn = Force/kbn;
dbw = Force/kbw;

if toggle == 0
    % total deflection narrow and wide
    dtotaln(k) = ds + dbn;
    dtotalw(k) = ds + dbw;
end
if toggle == 1
    % total deflection narrow and wide
    dtotaln(k) = ds + dbn;
    dtotalw(k) = ds + dbw;
end
if toggle == 2
    % total deflection narrow and wide
    dtotaln(kk) = ds + dbn;
    dtotalw(kk) = ds + dbw;
end
```

```
    if toggle == 0
        % calculate specific panel stiffness
        kpaneln(k) = (kbn + ks) / mass(k);
        kpanelw(k) = (kbw + ks) / mass(k);
    end
    if toggle == 1
        % calculate specific panel stiffness
        kpaneln(k) = (kbn + ks) / mass(k);
        kpanelw(k) = (kbw + ks) / mass(k);
    end
    if toggle == 2
        % calculate specific panel stiffness
        kpaneln(kk) = (kbn + ks) / mass(kk);
        kpanelw(kk) = (kbw + ks) / mass(kk);
    end

    % calculate core shear stress
    cshear(k) = 0.5*Force / (distance + width);            % core shear using hexcel formula
```

```
in psi
    if toggle == 0
        cshear_thesis(k) = 0.5*Force / ((thick+cthick(k))*width);  % core shear using simplif
ied beam theory proposed by Allen in psi
    end
    if toggle == 1
        cshear_thesis(k) = 0.5*Force / ((thick+cthick(k))*width);  % core shear using simplif
ied beam theory proposed by Allen in psi
    end
    if toggle == 2
        cshear_thesis(kk) = 0.5*Force / ((thick+cthick)*width);  % core shear using simplifie
d beam theory proposed by Allen in psi
    end

    % calculate elastic buckling stress
    cell_size = 3/16; % in in
    G_alu = 3.76e06; % in psi
    v_alu = 0.33;
    if toggle == 0
        sigma_c_el(k) = 12.1/(1-v_alu)*G_alu*(cthick(k)/cell_size)^3; % equation 11
    % source: Materials Science and Engineering A380
    % "out-of-plane compressive behavior of metallic honeycombs"
    % F. Cote, V.S. Deshpande, N.A. Fleck, A.G. Evans
    end

    if toggle == 1
        sigma_c_el(k) = 12.1/(1-v_alu)*G_alu*(cthick(k)/cell_size)^3;
    end

    if toggle == 2
        sigma_c_el = 12.1/(1-v_alu)*G_alu*(cthick/cell_size)^3;
    end
```

Build Load Vector

build thermal load vector

```
load_t = [N_t; M_t];
% combine mechanical and thermal loading
load = load_t + load_m;
```

Calculate Strains, Curvatures and Stresses

solve for strain and curvatures

```
e = C*load;

% initialize Stress Vector
stressxy = zeros(2*n,4);
strainxy = zeros(2*n,4);

% loop over each ply and calculate strain
for i = 1:n
    % loop over top and bottom of each ply
```

```
    % starting at the top of ply
    for j = 1:2
        %
        ply = i; % ply number
        loc = j; % location of the ply
                 % 1: top
                 % 2: bottom

        % ply material ID
        mi = L(i,3);
        v21 = M(mi,3)*M(mi,5)/M(mi,2);
        D_s = 1 - M(mi,5)*v21;

        % Q12 matrix
        Q = [M(mi,2)/D_s           v21*M(mi,2)/D_s    0;
            M(mi,5)*M(mi,3)/D_s  M(mi,3)/D_s        0;
            0                  0                M(mi,4)];

        % ply angle in radians
        theta = L(i,1)*pi/180;

        % Form transformation matrices T1 for each ply
        T1 = [(cos(theta))^2          (sin(theta))^2           2*sin(theta)*cos(theta);
              (sin(theta))^2          (cos(theta))^2          -2*sin(theta)*cos(theta);
              -sin(theta)*cos(theta)   sin(theta)*cos(theta)  (cos(theta))^2-(sin(theta))
^2 ];
```

```
        % form T2 for thermal
        T2 = R*T1*inv(R);
        % load alphas into an array
        a = [M(mi,6); M(mi,7); 0.0];
        % calculate thermal strains
        e_thermal = delT*inv(T2)*a;
        % Form Qxy
        Qxy = inv(T1)*Q*R*T1*inv(R);
        % calculate distance from midsurface
        z = h(i-1+j);
        % transform back to principal directions
        % global total strains
        e_tot_glo = [ e(1)+z*e(4);  e(2)+z*e(5);  e(3)+z*e(6)];
        % local total strains
        e_tot_loc = T2*e_tot_glo;
        % global mechanical strain
        e_m_glo = e_tot_glo - e_thermal;
        % local mechanical strain
        e_m_loc = e_tot_loc - e_thermal;

        % stresses only arise from mechanical strains
        % calculating stresses
        % global stresses
        stxy = Qxy*e_m_glo;
        % local stresses
        st12 = Q*e_m_loc;

    % uses MAX Strain criteria
    % failure index now looks at two different materials
    % check fiber direction
    if e_tot_loc(1) > 0.0;
```

```
        FI = e_tot_loc(1)/M(mi,13);
        FIF(1)=FI;
    elseif e_tot_loc(1) < 0.0;
        FI = abs( e_tot_loc(1) )/M(mi,16);
        FIF(1)=FI;
    end

    % check transverse direction
    if e_tot_loc(2) > 0.0;
        FIF(2) = e_tot_loc(2)/M(mi,14);
    elseif e_tot_loc(2) < 0.0;
        FIF(2) = abs( e_tot_loc(2) )/M(mi,17);
    end

    % check in-plane shear
        FIF(3) = abs( e_tot_loc(3) )/M(mi,15);

    % FIF is failure index on fiber failure
    % FIe is the highest failure index which could be fiber, transverse or
    % shear
```

```
            % display stresses and strains in a matrix
            % Write local Stress for each ply on top and bottom into a matrix
            stress12(2*i+j-2,1)=i;              % ply number
            stress12(2*i+j-2,2)=L(i);           % ply angle
            stress12(2*i+j-2,3)=st12(1);        % stress in 1 direction
            stress12(2*i+j-2,4)=st12(2);        % stress in 2 direction
            stress12(2*i+j-2,5)=st12(3);        % Shear stress in 12
            % Write total local Strain for each ply on top and bottom into a matrix
            strain12(2*i+j-2,1)=i;              % ply number
            strain12(2*i+j-2,2)=L(i);           % ply angle
            strain12(2*i+j-2,3)=e_tot_loc(1);   % strain in ply 1 direction
            strain12(2*i+j-2,4)=e_tot_loc(2);   % strain in ply 2 direction
            strain12(2*i+j-2,5)=e_tot_loc(3);   % strain in ply 12 or shear strain
            % Write global Stress for each ply on top and bottom into a matrix
            stressxy(2*i+j-2,1)=i;              % ply number
            stressxy(2*i+j-2,2)=L(i);           % ply angle
            stressxy(2*i+j-2,3)=stxy(1);        % stress in 1 direction
            stressxy(2*i+j-2,4)=stxy(2);        % stress in 2 direction
            stressxy(2*i+j-2,5)=stxy(3);        % Shear stress in 12
            % Write total global Strain for each ply on top and bottom into a matrix
            strainxy(2*i+j-2,1)=i;              % ply number
            strainxy(2*i+j-2,2)=L(i);           % ply angle
            strainxy(2*i+j-2,3)=e_tot_glo(1);   % stress in 1 direction
            strainxy(2*i+j-2,4)=e_tot_glo(2);   % stress in 2 direction
            strainxy(2*i+j-2,5)=e_tot_glo(3);   % Shear stress in 12
            % Write Failure Index into a matrix
            efail(2*i+j-2,1)=i;                 % ply number
            efail(2*i+j-2,2)=L(i);              % ply angle
            efail(2*i+j-2,3)=FIF(1);            % failure index longitudinal
            efail(2*i+j-2,4)=FIF(2);            % failure index transverse
            efail(2*i+j-2,5)=FIF(3);            % failure index shear
        end

    end
```

```
end
end
```

Print out the results

```
disp('The deflection of the panel for a narrow beam solution: ')
fprintf('%2.3f',dtotaln)
fprintf('\n')
disp('The deflection of the panel for a wide beam solution: ')
fprintf('%2.3f',dtotalw)
fprintf('\n')
disp('The D16 of the Laminate: ')
fprintf('%2.3f',D(1,3))
fprintf('\n')
disp('The D26 of the Laminate: ')
fprintf('%2.3f',D(2,3))
fprintf('\n')
```

```
The deflection of the panel for a narrow beam solution:
0.329
The deflection of the panel for a wide beam solution:
0.248
The D16 of the Laminate:
666.841
The D26 of the Laminate:
666.841
```

Plotting Core Thickness Graphs

```
if toggle == 1
```

Plot Deflection and Specific Stiffness

```
figure('Name','Stiffness Sensitivity' ,'NumberTitle','Off')
% yyaxis left
plot(cthick, dtotalw, 'b')
hold on
xlabel('Core Thickness [in]')
ylabel('Panel Deflection [in]')
% yyaxis right
% plot(cthick, kpanelw, 'r')
% ylabel('Specific Stiffness [lb*in2/lbm]')
% legend('Panel Deflection', 'Specific Stiffness', 'Location', 'NorthWest')
% hold off
```

Plot Elastic Buckling and Core Shear

```
figure('Name','Strength Sensitivity' ,'NumberTitle','Off')
yyaxis left
plot(cthick, sigma_c_el, 'b')
hold on
xlabel('Core Thickness [in]')
ylabel('Core Elastic Buckling Stress [psi]')
yyaxis right
plot(cthick, cshear, 'r')
ylabel('Core Shear Stress [psi]')
legend('Elastic Buckling Stress', 'Core Shear Stress', 'Location', 'NorthWest')
hold off
```

```
end
```

PLotting Ply Thickness Graph

```
if toggle == 2
```

Plot Deflection

```
figure('Name','Stiffness Sensitivity' ,'NumberTitle','Off')
% yyaxis left
plot(pthick, dtotalw, 'b')
hold on
xlabel('Ply Thickness [in]')
ylabel('Panel Deflection [in]')
% yyaxis right
% plot(pthick, kpanelw, 'r')
% ylabel('Specific Stiffness [lb*in2/lbm]')
% legend('Panel Deflection', 'Specific Stiffness', 'Location', 'NorthWest')
% hold off
```

```
end
```

Published with MATLAB® R2016a